

Shallow seismic structure of Kunlun fault zone in northern Tibetan Plateau, China: implications for the 2001 *M*s8.1 Kunlun earthquake

Chun-Yong Wang,¹ Walter D. Mooney,² Zhifeng Ding,¹ Jiansi Yang,¹ Zhixiang Yao¹ and Hai Lou¹

¹Institute of Geophysics, China Earthquake Administration, Beijing 100081, China E-mail: wangcy@cea-igp.ac.cn

²US Geological Survey, Menlo Park, CA 94025, USA

Accepted 2008 November 12. Received 2008 November 11; in original form 2007 October 10

SUMMARY

The shallow seismic velocity structure of the Kunlun fault zone (KLFZ) was jointly deduced from seismic refraction profiling and the records of trapped waves that were excited by five explosions. The data were collected after the 2001 Kunlun *M*s8.1 earthquake in the northern Tibetan Plateau. Seismic phases for the in-line record sections (26 records up to a distance of 15 km) along the fault zone were analysed, and 1-D *P*- and *S*-wave velocity models of shallow crust within the fault zone were determined by using the seismic refraction method. Sixteen seismic stations were deployed along the off-line profile perpendicular to the fault zone. Fault-zone trapped waves appear clearly on the record sections, which were simulated with a 3-D finite difference algorithm. Quantitative analysis of the correlation coefficients of the synthetic and observed trapped waveforms indicates that the Kunlun fault-zone width is 300 m, and *S*-wave quality factor *Q* within the fault zone is 15. Significantly, *S*-wave velocities within the fault zone are reduced by 30–45 per cent from surrounding rocks to a depth of at least 1–2 km, while *P*-wave velocities are reduced by 7–20 per cent. A fault-zone with such *P*- and *S*-low velocities is an indication of high fluid pressure because *V*_s is affected more than *V*_p. The low-velocity and low-*Q* zone in the KLFZ model is the effect of multiple ruptures along the fault trace of the 2001 *M*s8.1 Kunlun earthquake.

Key words: Controlled source seismology; Guided waves; Fractures and faults; Crustal structure; Asia.

1 INTRODUCTION

The internal properties of active fault zones are of great interest to seismologists who study the earthquake source and to geologists who investigate the deformation of the crust in response to regional stresses (Aki 1979; Kanamori 1994). Several recent reviews have demonstrated that an improved knowledge of the detailed physical properties of a major fault zone can be used to improve the understanding of earthquake processes and the long-term evolution of a fault (Aki & Richards 2002; Scholz 2002; Sibson 2002; Lyakhovsky & Ben-Zion 2008). An opportunity to study the shallow seismic structure of an active fault was presented by the Kunlun *M*s8.1 earthquake of 2001 November 14, which occurred in the northern Tibetan Plateau (Fig. 1a). This earthquake generated a rupture zone with a total length of 426 km oriented in a nearly E–W direction along the southern piedmont of the Kunlun Mountains, with the Kekexili Plateau to the south. The epicentre is located at (36.2°N, 90.9°E), and the focal depth is 15 km (Institute of Geophysics, CSB 2002). The seismic fault-plane solution from moment tensor inversion indicates left-lateral strike-slip with a dip-angle of 85° and a slip-angle of –10° (Xu & Chen 2005). Field geological surveys indicate that the macroscopic epicentre is located in the southern

piedmont of the Kunlun Mountains, to the northeast of the Hoh Sai Lake, and about 80 to 90 km west of the Kunlun Pass. They also indicate that the surface rupture is predominated by left-lateral strike-slip with a maximum slip of 7.6 m (Lin *et al.* 2002b; Van der Woerd *et al.* 2002; Xu *et al.* 2002).

The shallow structure of a major fault zone can be explored in several ways, including active-source seismic profiling, seismic tomography (Louie *et al.* 1988; Lees & Malin 1990; Thurber *et al.* 1997) and fault-zone trapped waves (Li & Leary 1990; Li *et al.* 1999; Ben-Zion *et al.* 2003; Lewis *et al.* 2005). A number of seismic experiments have been carried out at the site of rupture zones generated by recent destructive earthquakes, such as the Parkfield segment of the San Andreas fault (Li *et al.* 2004; Li *et al.* 2006), the 1992 *M*s7.5 Landers earthquake (Li *et al.* 1994, 1999; Peng *et al.* 2003), the 1995 *M*s7.2 Kobe earthquake (Li *et al.* 1998), the 1999 *M*7.1 Hector Mine earthquake (Li *et al.* 2002a) and the 1999 *M*w7.4 Izmit earthquake (Ben-Zion *et al.* 2003). These studies of the fault-zone internal structure have shown that major crustal faults are generally characterized by seismic low-velocity zones with width of a few hundred metres to a few kilometres. Such low-velocity zones are considered to be caused by an unknown combination of fluid concentration near faults, clay-rich fault gouge, increased

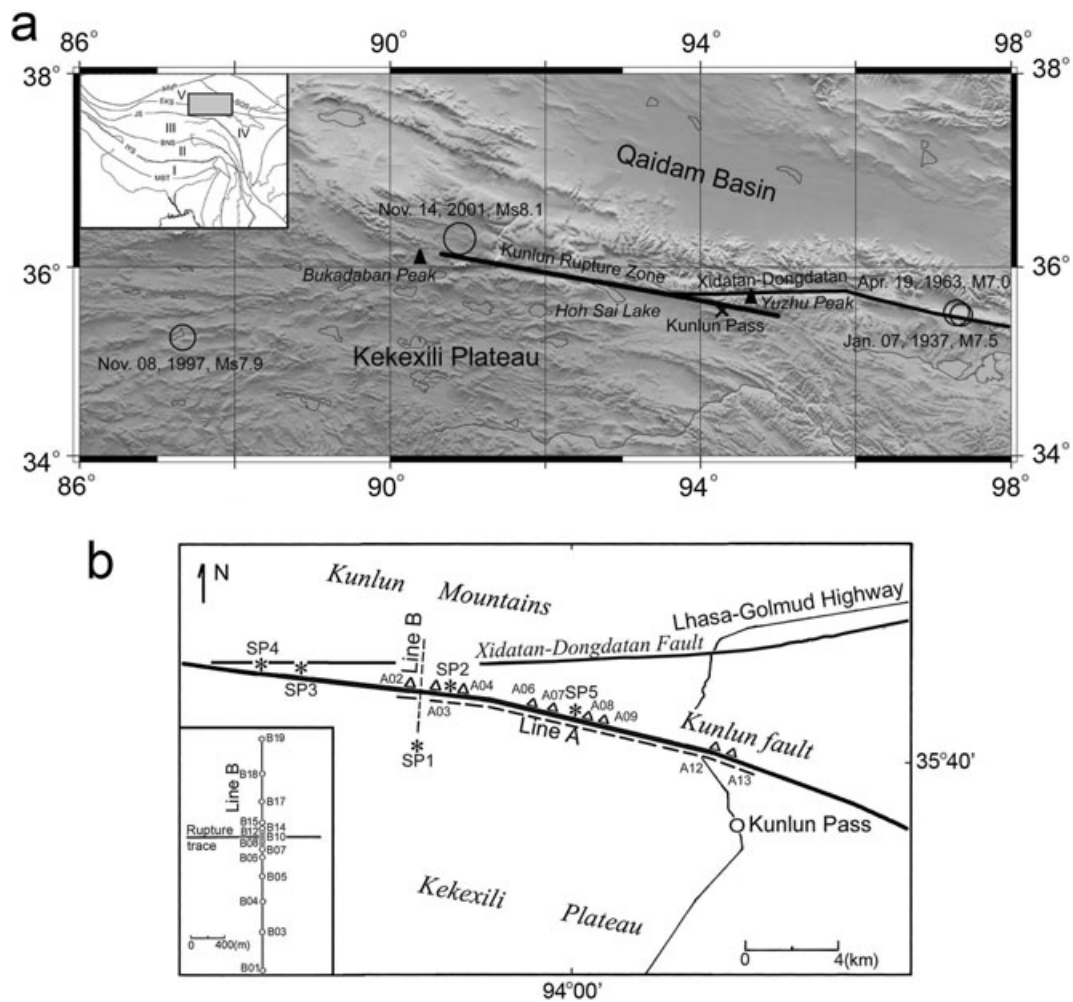


Figure 1. (a) Topography of the northern Tibetan Plateau and location of the eastern Kunlun fault zone. Dark line indicates the rupture zone generated by the 2001 Kunlun earthquake. The circles denote the 2001 Kunlun earthquake and strong earthquakes occurred in the 20th century. The inset tectonic map of the Tibetan Plateau is simplified from Yin & Harrison (2000), where I, Himalaya block; II, Lhasa block; III, Qiantang block; IV, Songpan-Ganzi complex and V, Qaidam block. IYS: Indus–Yarlung Zangbo Suture; BNS: Bangong–Nijiang Suture; JS: Jinsha river Suture, EKS: Eastern Kunlun Suture and SQS: South Qilian Suture. (b) Map of the field experimental site and seismic profiles showing five shot points (SP1, SP2, SP3, SP4 and SP5), two linear seismic arrays (Line A and Line B shown by dotted lines). Line A consists of 13 stations (open triangles). The inset diagram shows the geometry of the dense linear array on Line B, where the open circles with station code denote station locations. Due to instrument malfunction, stations A01, A05, A10 and A11 on Line A and stations B02 and B16 on Line B did not receive any data.

porosity and crack dilatation that may occur during the earthquake rupture process (Thurber 1983; Cormier & Spudich 1984; Mooney & Ginzburg 1986; Li & Leary 1990; Ben-Zion 1998; Ben-Zion & Sammis 2003). Recent borehole measurements (Hickman *et al.* 2005) confirm that densely fractured rocks associated with active faults have significantly reduced velocities. Thus, there is a correlation between fault slip behaviour and seismic velocity structure within the fault zone.

Two months after the 2001 Kunlun earthquake, a 32-station broad-band seismic network was deployed along and across the surficial rupture trace in the eastern segment of the Kunlun rupture zone, and collected seismic records excited by explosions (Fig. 1b). The objective of this seismological experiment is to image the shallow structure of the fault zone using both seismic *P*- and *S*-refracted waves, and trapped waves propagating in the low-velocity damaged fault zone. The eastern segment of the Kunlun fault zone (KLFZ), from the Hoh Sai Lake to the Kunlun Pass, corresponds to the main surface rupture, and also to the most active aftershock zone of the 2001 Kunlun earthquake (China Seismological Bureau 2003). This

experimental site was also selected based on the simplicity of the near-surface geology. The fault rupture here broke the surface in bedrock, avoiding possible complications due to sedimentary layers that can diffuse and mask signals propagating within the fault zone. In this paper, based on the analysis of the refracted phases and the trapped waves produced by explosive shots and recorded by linear seismic arrays along and across the Kunlun rupture zone, the shallow seismic structure of the fault zone is jointly presented by means of numerical simulations of the fault-zone trapped waves and interpretation of the refracted waves.

2 REGIONAL GEOLOGIC SETTING AND PREVIOUS GEOPHYSICAL STUDIES

The Tibetan Plateau has been uplifted over the past 45 Ma by the collision of the Indian and Eurasian plates. From south to north, the Tibetan Plateau can be divided into six tectonic units: Himalaya block, Lhasa block, North Tibetan block, Qiantang block, Songpan–Ganzi Complex and Qaidam block (Fig. 1a, inset map, Yin &

Harrison 2000). The eastern Kunlun suture, formed in the latest Triassic and early Jurassic, is a boundary between the Songpan–Ganzi Complex and the Qaidam block of the northernmost Tibetan Plateau. In response to the N–S compression stresses on the plateau, tectonic movement has been manifested along the southern edge of the Kunlun mountain belt (Qinghai Seismological Bureau & Institute of Geodynamics, CSB 1999). The eastern KLFZ (Fig. 1a) accommodates left-lateral strike-slip motion along the eastern Kunlun suture, and has undergone both strike-slip and compression deformation during the Quaternary period. Several papers (Kidd & Molnar 1988; Van der Woerd *et al.* 1998, 2000) elaborated the modern tectonic activity of the eastern KLFZ.

In this paper, the KLFZ specifically refers to the eastern segment of the eastern KLFZ, from the Hoh Sai Lake to the east of the Kunlun Pass (Fig. 1a). KLFZ is an active fault zone resulting from thrust faulting in the Late Pliocene associated with the compression and uplift of the Tibetan Plateau. In a process known as escape tectonics, the primary kinematics of thrust faulting was transformed into left-lateral strike-slip motion by the end of the early Pleistocene. The newly generated surface rupture can be observed as an overprint on the palaeo-earthquake deformation zones at some sites (Qinghai Seismological Bureau & Institute of Geodynamics, CSB 1999; Van der Woerd *et al.* 2000). In the 20th century, several strong earthquakes with magnitude greater than 7.0 (i.e. the 1937 Tusuo $M7.5$ earthquake, the 1963 Alag $M7.0$ earthquake and the 1997 Manyi $M7.9$ earthquake shown in Fig. 1) occurred, resulting in rupture on the KLFZ or nearby faults. During the 1990s, several geological and seismological studies were conducted on these earthquakes (Van der Woerd *et al.* 1998; Peltzer *et al.* 1999; Qinghai Seismological Bureau & Institute of Geodynamics, CSB 1999; Xu & Chen 1999).

Geologic field surveys confirmed that the surface rupture of the 2001 Kunlun earthquake tended to follow the pre-existing palaeo-earthquake fault zone (Xu *et al.* 2002). This fault initiates near the Bukadaban Peak (36.0°N, 90.5°E) in the west, and extends eastwards through the Hoh Sai Lake, south of the Yuzhu Peak, and terminates about 70 km east of the Kunlun Pass (35.4°N, 95.2°E). The surface rupture generally trends N80°–85°W (Fig. 1) and is mainly situated on the eastern segment with length of 350 km. East of the Kunlun Pass, the KLFZ is divided into two branches, where the north branch is known as the Xidatan–Dongdatan segment and the south branch coincides with the rupture generated by the 2001 Kunlun earthquake.

A temporary seismic network was deployed south of Golmud to monitor the seismicity from 2001 November 19 to 2002 April 6. A total of 3987 aftershocks with magnitude greater than 1.0 were recorded during this period (China Seismological Bureau 2003). The data demonstrate that the eastern segment of KLFZ is an area with dense aftershock distribution.

Prior to the 2001 Kunlun earthquake, active-source deep seismic refraction profiles and a comprehensive suite of non-seismic geophysical measurements were carried out on two north–south stretching Geoscience Transects across the southern Tibetan Plateau (from Yadong to Golmud, Wu *et al.* 1991) and the northern Tibetan Plateau (from Golmud to E'jin Qi, Cui *et al.* 1995). The 2-D crustal structures along these transects indicate that crustal thickness beneath the Kunlun Mountains is about 50 km. In addition, lateral variations in the structure of the crust of the northern Tibetan Plateau have been inferred from teleseismic receiver functions (Zhu *et al.* 1995). Despite the existence of these data, there has been limited reliable information regarding the shallow seismic velocity structure of the crust in the vicinity of KLFZ.

Table 1. Locations of shot points.

Name of shot point	Latitude (N)	Longitude (E)	Elevation (m)
SP1	35°39.888'	93°55.535'	4784
SP2	35°41.392'	93°56.738'	4868
SP3	35°41.577'	93°52.364'	4887
SP4	35°41.603'	93°51.825'	4915
SP5	35°40.724'	94°01.067'	4795

3 EXPLORATION OF THE SHALLOW STRUCTURE OF KLFZ

The large-scale rupture zone associated with the 2001 Kunlun earthquake provides an attractive target of the investigation of the internal structure of a major continental strike-slip fault. For this reason, an active seismic experiment using explosive sources was conducted in 2002. The field site is situated on the eastern segment of the surface rupture, extending westwards about 15 km from the Kunlun Pass (Fig. 1b).

3.1 Geometry of the seismic refraction experiment

Several papers elucidated the fault-zone trapped waves that are generated by earthquake or explosive source and recorded by seismographs distributed over the fault zone (e.g. Li *et al.* 1999; Ben-Zion *et al.* 2003; Lewis *et al.* 2005). In the KLFZ field experiment, 32 temporary seismic stations were deployed along two profiles, Line *A* and Line *B* (Fig. 1b). Line *A* consists of 13 stations parallel to the rupture zone and is about 20 km in length. A denser linear seismic array of 19 stations was deployed on Line *B*, which is perpendicular to the rupture zone and is about 3 km long. The geometry of Line *B* is shown in the inset map of Fig. 1(b), where the central station (B10) is closest to the rupture trace. Stations were unevenly distributed, with an interval of 30 m in the central part and gradually increasing outwards to 300 m at the two ends of the profile. The three-component seismographs with hard disk memory were deployed, where the seismometers have a frequency band from 20 s to 40 Hz (Zhao *et al.* 1997). There are five explosions in the experiment (Table 1), each of which was fired in boreholes at depths of about 25 m, with explosive charges of 250 kg. Except for SP1, which is located outside the fault zone, 2.7 km from the rupture trace, shot points are located within the fault zone, some 20 m or less from the rupture trace (Fig. 1b). Seismic waves excited by explosions were simultaneously recorded at stations on Line *A* and Line *B*. All recorders and shots were synchronized through GPS clocks, and timing errors are smaller than 0.01 s. The sampling interval on records is 10 ms. The experiment was carried out under adverse field conditions. Temperature in the experimental site decreased below –15°C, and some hard disks malfunctioned.

3.2 Traveltime analysis of *P* and *S* arrivals on the record sections

3.2.1 In-line record sections along fault zone (Line *A*)

In the field experiment, out of 13 stations on Line *A*, the instruments at only six or seven stations worked normally. In view of limited amount of arrival-time data from individual shot, the records at the stations along the fault zone from all four shots on Line *A* were merged into a data file, and a composite record section was plotted based on the shot-receiver distance. The vertical and radial component record sections (Figs 2a and b) contain 26 records with

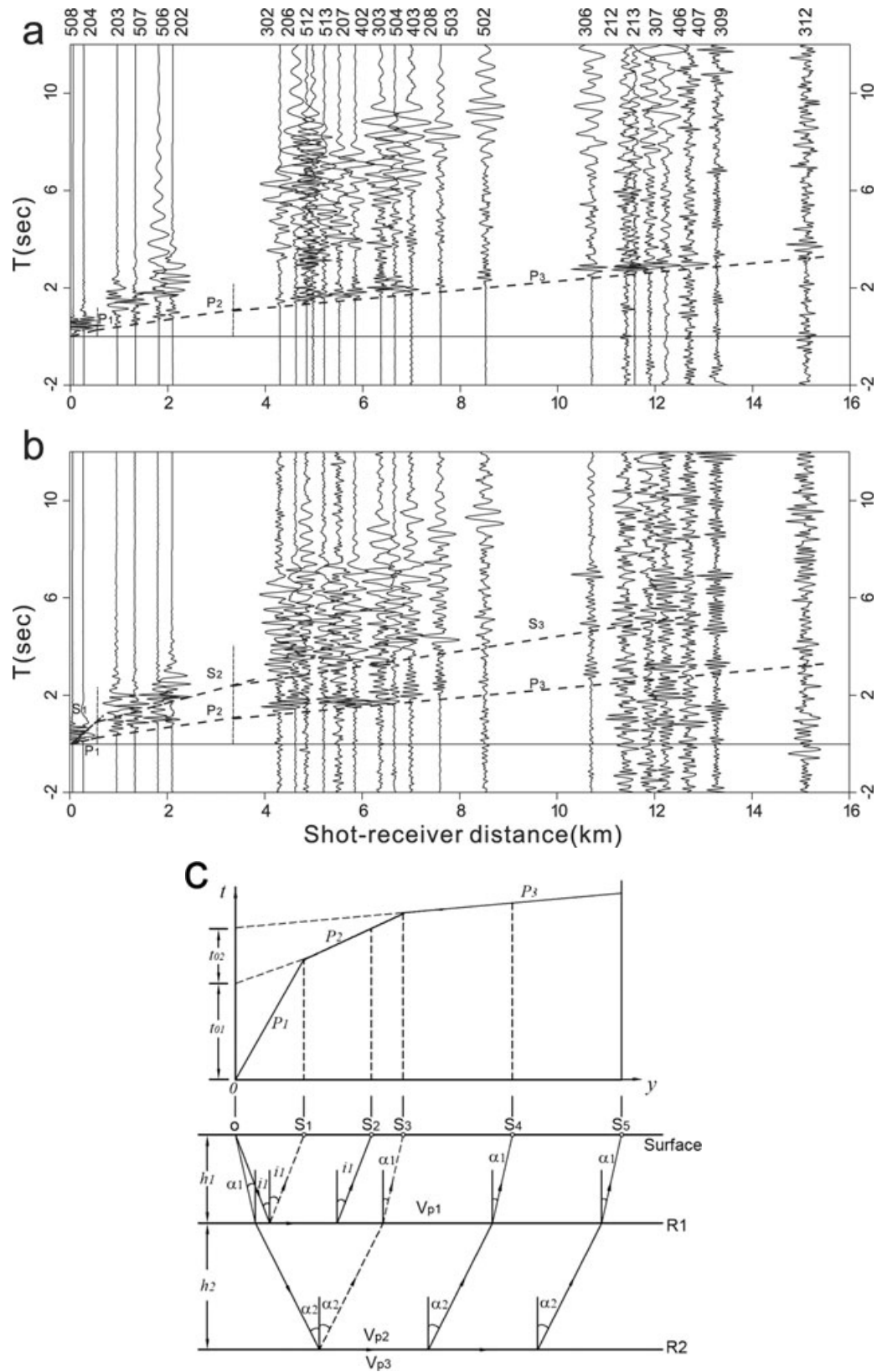


Figure 2. (a) Trace-normalized vertical-component record section on Line *A* (parallel to the fault zone). The station number is marked at the top of each trace, where the first numeral represents shot number and the following two numerals are station number. The direct and refraction phases are marked by thick dotted line. (b) Trace-normalized radial-component record section on Line *A*. Thick dotted lines denote the first *P* arrivals (*P*₁, *P*₂ and *P*₃) and *S* arrivals (*S*₁, *S*₂ and *S*₃), which are marked on the vertical and radial record sections. The radial component is in the fault-parallel direction. (c) Sketch map of time-distance graph of arrivals *P*₁, *P*₂ and *P*₃, and related ray paths in a three-layer model ($V_{p3} > V_{p2} > V_{p1}$). *P*₁ is a direct wave. *P*₂ and *P*₃ are head waves along interfaces *R*₁ and *R*₂, respectively.

relatively small receiver spacing. The radial component is in the fault parallel direction. The merging of all recordings from the four shots is justified by assuming the lateral homogeneity within a small interval of 15 km on Line *A*. The resulting composite section provides a measurement of the average traveltimes of the uppermost crust along the profile. Although the near-surface geology at the sites of four shots close to the fault zone is not completely identical, traveltimes of each phase are consistent with each other. Spectral analysis of the waveforms indicates that the body waves (both *P* and *S*) excited by these shots fall into the frequency range of 4–10 Hz.

The interpretative method for deep seismic sounding (Giese & Prodehl 1976; Meissner 1986; Mooney 1989; Holbrook *et al.* 1992; Wang *et al.* 2007) was applied to the record sections (Figs 2a and b), similar to the analysis of Ben-Zion & Malin (1991). As usual, the first arrivals on the record section of vertical component are recognized as shallow crustal *P*-wave refractions. Fig. 2(c) illustrates the seismic phases observed on the record sections in Figs 2(a) and (b). The *P*-wave velocity structure can be determined from *P*-wave first arrivals by using the ray tracing method for head waves or diving waves (Cerveny & Psencik 1984). In this manner, the *P*-wave first arrivals were inverted for a 1-D *P*-wave three-layer velocity model to a depth of about 5 km.

Depending on the seismic source used, active-source record sections do not always present *S*-wave arrivals. However, some record sections of deep seismic sounding profiles conducted in different geologic settings show clear *S*-wave arrivals (Braile *et al.* 1974; Assumpcao *et al.* 1978; El-Isa *et al.* 1987; Holbrook *et al.* 1988; Wang *et al.* 2000). A generally acceptable explanation for the *S*-wave phases is that the Earth's free surface generates converted *P*–*S* waves from an explosive point source (Fertig 1984). The *S*-wave arrivals are distinct on horizontal-component records of both in-line and off-line record sections in Figs 2–4. After the first *P* arrivals on the vertical-component section were well defined (Fig. 2a), the corresponding *S* arrivals on the radial-component section can be traced (Fig. 2b), and then both the 1-D *P*- and *S*-wave velocity models were determined. The *S*-wave phases are, of course, secondary arrivals and so the accuracy of *S*-arrival pickings is lower than that of the first *P* arrivals due to interference with the *P*-wave coda.

Asymptotic ray theory (Cerveny & Psencik 1984) was used to calculate theoretical traveltimes of the seismic phases, and a comparison was made with observed traveltimes. Ray tracing was carried out in the 1-D models, where the refracted phases were simulated by diving waves travelling in a layer with a slight velocity gradient. This scheme was used to refine the layer's seismic velocity and thickness for a layered velocity structure. The 1-D *P*- and *S*-wave velocity structures along Line *A*, determined by ray tracing, are shown in Table 2, where the third layer is semi-infinite. The rms traveltime residuals are 0.05 and 0.11 s for *P* and *S* arrivals, respectively.

3.2.2 In-line record sections from shot SP1

Out of the 19 stations deployed on Line *B*, the seismographs at 17 stations worked. Fig. 3(a) shows the three-component in-line record sections on Line *B* from shot SP1. On the record sections, the first *P* arrival and *S* arrival are marked as P2 and S2, in agreement with the nomenclature used for the phases on Line *A* (Figs 2a and b). The apparent velocity of phase P2 is 4.4 km s⁻¹ at distances from 1.2 to 2.4 km, and then decreases to 4.0 km s⁻¹ from 2.4 to 2.8 km. The phase S2 has an apparent velocity of 2.8 km s⁻¹ at distances from 1.2 to 2.4 km, and 2.1 km s⁻¹ from 2.4 to 2.8 km (Fig. 3a). Phases

P2 and S2 are designated as the refractions from the second layer at distances from 1.2 to 3.6 km, following the analysis of record sections along Line *A* (Figs 2a and b). The apparent velocities of P2 and S2 were adopted as the velocities in the second layer outside the fault zone in the initial 3-D model of KLFZ.

Fig. 3(b) shows the vertical- and radial-component record sections for six stations on Line *B* that are 100 m or more south of rupture trace and three stations on Line *A*. Thus, the greater part of the ray path of all phases lies outside the fault zone. In comparison with the phases (P2, P3 and S2, S3) within the fault zone (Figs 2a and b), the arrivals on this section appear early, which means that the velocities of both *P* and *S* waves outside the fault zone are faster than that within the fault zone. In addition, the oscillatory shear wave trains after the *S* arrival in the seismograms are observed.

3.3 Waveform analysis of fault-zone trapped waves

On the in-line record sections along the fault zone (Line *A*), distinct seismic arrivals with a high-amplitude, low-frequency and long-wave train appear after the *S* arrival (Figs 2a and b). This wave train has been recognized as fault-zone trapped waves (Li & Leary 1990; Ben-Zion 1998). Besides on Line *A*, the stations on Line *B* also recorded the seismic waves excited by four shots (SP2, SP3, SP4 and SP5), which are at distances of 2.1, 4.8, 5.5 and 8.5 km from Line *B*, respectively (Fig. 1b). Off-line three-component record sections on Line *B* are shown in Fig. 4, where the stations were arranged in even record interval (same arrangement is used in further figures) and the real station locations are shown in the inset map of Figs 1(b) and 3(a). As seen on Line *A*, a high-amplitude, low-frequency wave train appears after the *S* arrivals in the vertical-component sections on Line *B*. Similar waveform features of the phases present on the radial-component sections, where the shear-wave phases (refractions and reflections) are clearly observed. Detailed analysis and numerical modelling of the phases will be described in the following sections.

Differing from an earthquake at a definite depth which causes fault-zone trapped waves, an explosion simultaneously creates Rayleigh waves, also called ground roll, and fault-zone trapped waves. Within the low-velocity fault zone, energy of the ground roll is much smaller than that of the trapped waves, as discussed in Section 5.2. Thus, the distinct arrivals with high-amplitude, low-frequency and long-wave train after the *S* arrival on both in-line and off-line record sections are called the trapped waves in this paper.

3.3.1 Amplitude spectra of trapped waves

The amplitude spectra on the records with sampling interval of 10 ms (i.e. 100 samples per second for Fourier transformation) were calculated for a 10 s time window starting from the *S* arrivals, using a Hanning window with a 50-ms taper. The arrival times of the *S* phase are related to shot-receiver distance (Fig. 2b), and depend upon the 1-D velocity model (Table 2). Amplitude spectra of coda waves were also calculated in a time window with the same length of 10 s, and starting 15 s after the *S* arrivals. The amplitude spectra were normalized using coda waves, so that site and source effects on the spectral amplitudes were eliminated (Li *et al.* 1999).

Figs 5(a)–(e) show the amplitude spectra of vertical-component records on Line *B* from shots SP2, SP3, SP4, SP5 and SP1. The records at stations on Line *B* constitute off-line profiles for shots SP2, SP3, SP4 and SP5, while they constitute in-line profile for SP1. The spectral peaks are located at 1.8–2.0 Hz for shots SP3 and

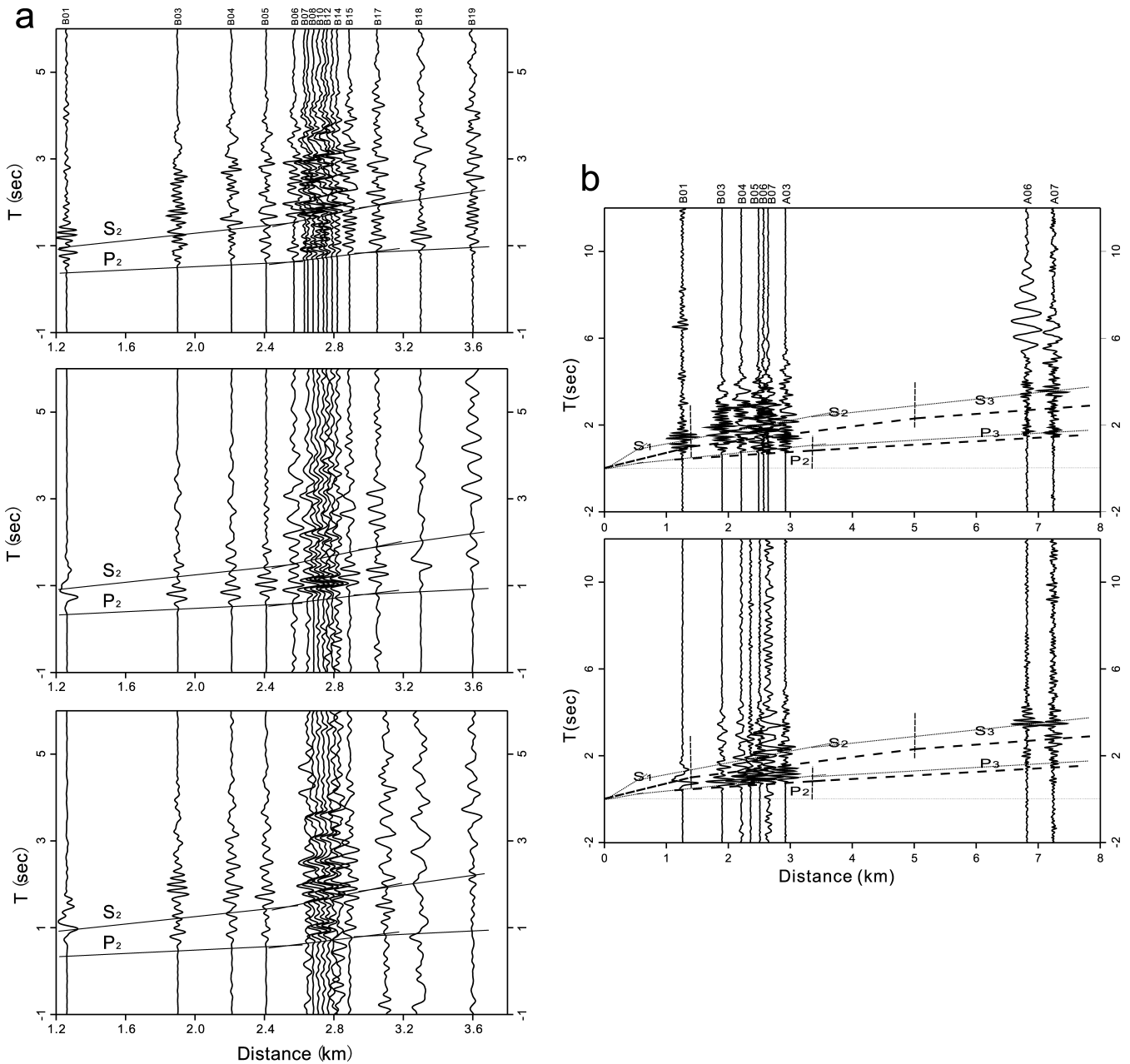


Figure 3. (a) Trace-normalized three-component record sections on Line *B* from shot SP1, which is located outside the fault zone. Upper panel: vertical component; Middle: radial component and lower panel: transverse component. The station number is marked at the top. Phases P2 and S2 are refracted waves, which are in agreement with the nomenclature used for the phases on Line *A* in Figs 2(a) and (b). (b) Trace-normalized record sections outside the fault zone, which are excited by shot SP1 and recorded at stations on Line *A* or Line *B*. The station number is marked at the top of each trace, where the first letter denotes the line. Upper panel: vertical component and lower panel: radial component. For comparison, the phases within and outside the fault zone are, respectively, denoted by light lines and thick dotted lines, and relevant phase marks P2, P3 and S1, S2, S3 have the same meaning as that in Fig. 2(b).

SP4 (Figs 5b and c). For shot SP5, the spectral peaks are located at 1.9–2.1 Hz, whereas another arrival appears behind the trapped waves, with spectral peak at 1.4–1.6 Hz (Fig. 5d). For shot SP2, the peaks of spectral aspect are broader and located at about 2.0 Hz at stations north of the rupture trace, but they are not dominant at 2.0 Hz at stations south of the rupture trace where there is another peak at about 3.0 Hz (Fig. 5a).

In general, the coda-normalized amplitude spectra of records on Line *B* from the shots within the fault zone are characterized by spectral peaks at about 2.0 Hz, as evidenced by the stations close by the rupture trace. The amplitude spectra at frequencies

<2.5 Hz could therefore be regarded mainly as the result of trapped waves. This implies that the seismic energy at frequencies <2.5 Hz is concentrated within the KLFZ. The coda-normalized amplitude spectra at stations B06 to B15 for four shots (Figs 5a–d) show a high degree of consistency, an observation that lends further support to their interpretation as the trapped waves (Li *et al.* 1999).

The amplitude spectra of vertical-component records from 3.2 to 4.2 s at stations on Line *B* from shot SP1 (Fig. 5e) have peaks at 1.3–1.6 Hz except for the records at stations B17–B19, where the peaks are irregularly distributed. Figs 5(a)–(e) manifest that the peaks of the spectra from in-line section are much broader than

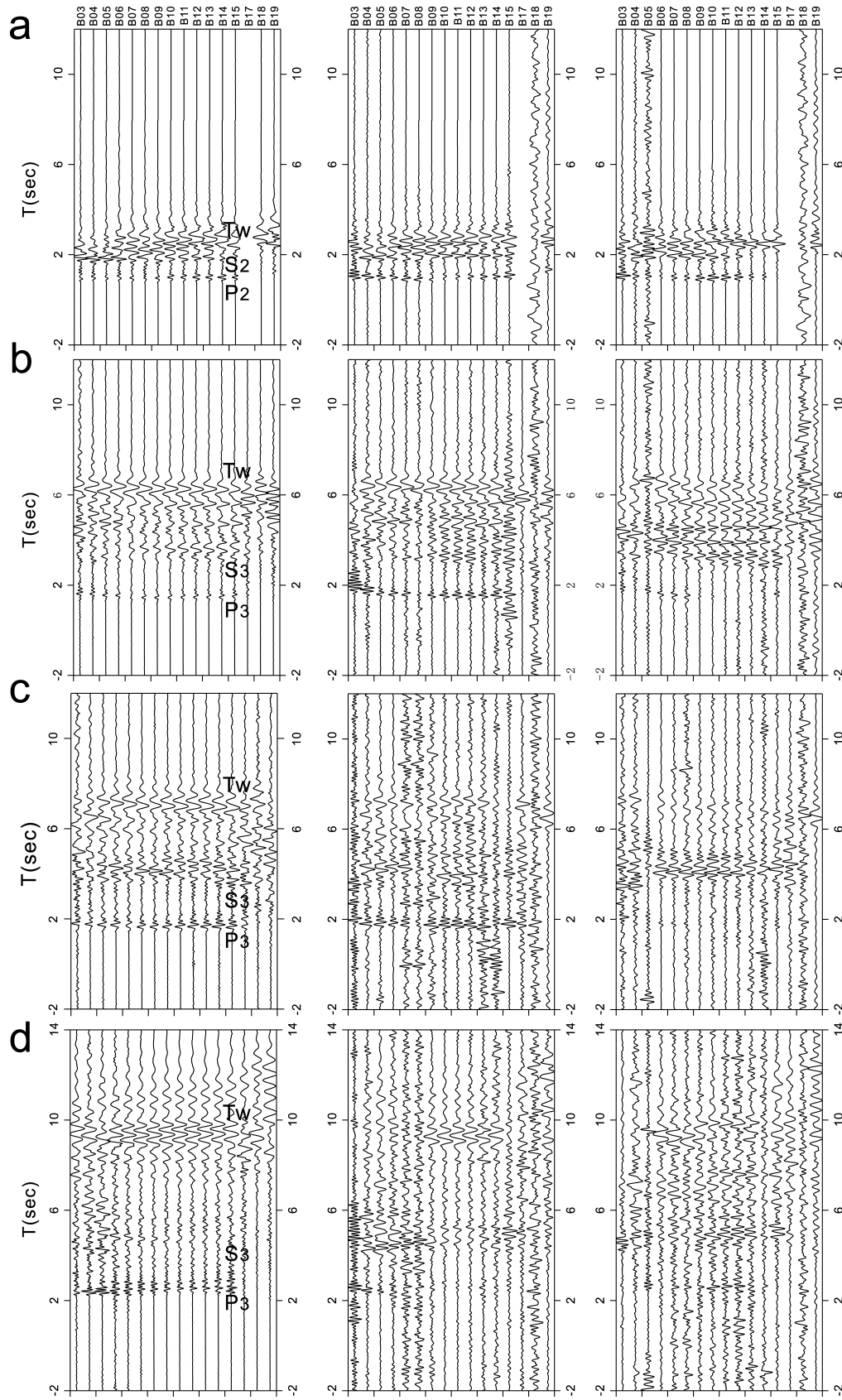


Figure 4. Trace-normalized three-component record sections with even trace interval from shots (a) SP2, (b) SP3, (c) SP4 and (d) SP5. These sections are plotted along the off-line profile (Line B). Real station locations are shown in the inset map of Figs 1(b) and 3(a). *T_w* denotes the trapped waves. P₂, S₂, P₃, S₃ are *P*- and *S*-refracted waves from the layer 2 and layer 3, respectively. Left-hand panel: vertical component, central panel: radial component and right-hand panel: transverse component.

Table 2. 1-D velocity structure along Line *A*.

No.	Depth interval (km)	P velocity (km s ⁻¹)	S velocity (km s ⁻¹)	V_p/V_s
1	0.00–0.40	2.30	1.07	2.15
2	0.40–1.05	4.03	1.92	2.09
3	1.05–5.00*	5.35	2.62	2.03

Asterisk denotes semi-infinite layer.

those from off-line sections. The peaks below 2.0 Hz in the spectra on Line *B* from shot SP1 can be considered as those of the ground roll.

The coda-normalized amplitude spectra of vertical-component records at stations on Line *A* are shown in Fig. 6(a) (right-hand panel), where the spectral peaks of about 2.0 Hz appear at distances from 1.5 to 13.0 km.

3.3.2 Dispersion of the trapped waves

Velocity dispersions were calculated using time-frequency analysis based on a multiple filter technique (Dziewonski *et al.* 1969). A four-pole Butterworth filter (two way type) was used to analyse the velocity dispersion of fault-zone trapped waves. Fig. 6(a) (left-hand and central panels) shows the trace-normalized record sections for the trapped waves filtered with lower frequency bands of 0.8–1.0 and 1.4–1.6 Hz on Line *A*, respectively. According to the dispersive characteristics of trapped waves shown in Fig. 6(a), it is obvious that the trapped waves at lower frequencies travelled faster than those at higher frequencies. The same waveform character of the trapped waves is observed in the records on Line *B* from shots SP2 to SP5. Fig. 6(b) shows the filtered record sections on Line *B* from shot SP3 filtered in three frequency bands with bandwidth of 0.3 Hz and central frequency of 0.95, 1.45 and 1.95 Hz, respectively. Again, it is obvious that the trapped waves at lower frequencies (0.8–1.1 Hz) travelled faster than those at higher frequencies (1.8–2.1 Hz).

To illustrate the dispersion of the trapped waves, we calculated the envelope of bandpass filtered seismograms at the stations on Line *A* from four shots by using the Hilbert transformation. Fig. 6(c) shows the waveform and relevant envelopes of bandpass-filtered records at station A03 from shots SP2 to SP5. The seismic records were filtered using a bandpass filter with a bandwidth of 0.2 Hz and a central frequency varying from 0.5 to 2.9 Hz in increments of 0.2 Hz. The peak of the envelope indicates the arrival of trapped energy at the specified frequency band.

Based on the position of the envelope peaks (Fig. 6c), the time difference between the arrivals of *S* waves (Fig. 2b) and those of the trapped waves increases with shot-receiver distance. This is due to the fact that *S* waves propagate at a velocity of 2.62 km s⁻¹ (Table 2), which is greater than the group velocities (<1.92 km s⁻¹) of the trapped waves, analysed in the next section.

3.3.3 Measurement of group velocity and its inversion

The group velocities of the trapped waves were measured from multiple bandpass-filtered seismic records at stations along and across the fault zone. The effect of the seismometer response on the trapped waves was removed by deconvolution (Li *et al.* 1999). The group velocities (with standard deviation) were calculated at frequencies between 0.5 and 2.5 Hz with increment of 0.1 Hz along and across the fault zone from shots SP1 to SP5, respectively, where the standard deviation at a specific frequency was determined from

multiple dispersion curves of the shots. The group velocities shown in Fig. 7(a) are the average of the group velocities measured at stations on Line *A* at individual frequencies. The group velocity ranges from 1.5 km s⁻¹ at 0.5 Hz to 0.8 km s⁻¹ at 2.5 Hz for shots SP2 to SP5, which are generally smaller than those of shot SP1. The standard deviation is smaller than 0.3 km s⁻¹ at frequencies >0.8 Hz, but some are larger than 0.3 km s⁻¹ at low frequencies (<0.8 Hz). Fig. 7(b) shows the group velocities, again based on the average of the group velocities at individual frequencies, measured at eight stations close by the rupture trace on Line *B*. The group velocities across the fault zone are similar to those along the fault zone to a great extent, but are slightly different at some frequencies for a specific shot, for example, SP2.

Based on the measured group velocities (Fig. 7a), the *S*-wave velocity structure was inverted using a genetic algorithm (Sambridge & Drijkoningen 1992). The thickness of each layer was fixed to 0.1 km and only *S*-wave layer velocity was inverted. *P*-wave velocity and density were calculated from the *S*-wave velocity by using empirical relationships (Christensen & Mooney 1995). The genetic algorithm produced a range of velocity models whose misfits lie within the uncertainties of group velocity measurements. Fig. 7(c) shows the 1-D velocity structure inverted from group velocity measurements of shot SP1, where the theoretical group velocities were calculated by using the Haskell matrix method (Aki & Richards 2002). The dispersion from shot SP1 is considered to be the effects of ground roll.

3.3.4 Estimate of the *S*-wave quality factor *Q*

The spectral ratio method (Teng 1968) was used to estimate the *S*-wave quality factor *Q* within and outside the fault zone on the understanding that the two stations simultaneously received seismic waves excited by two shots in the KLFZ experiment. The spectral ratio between two stations from one shot and the spectral ratio between two shots at one station are firstly formularized. These two spectral ratios are then used to form an equation to solve the *Q* value at a specific frequency.

The relationship between surface-wave spectral amplitude $A(r)$ and attenuation Q is

$$A(r) = A_0 D(r) \exp\left(-\frac{\omega}{2CQ}r\right) I(r),$$

where $A(r)$ and $A_0 = A(0)$ denote, respectively, the spectral amplitude at distance r and 0, ω is circular frequency, C is phase velocity, $D(r)$ is geometric attenuation factor and $I(r)$ is the factor related to station and instrument. For the two stations r_1 and r_2 , the spectral amplitude ratio between $A(r_1)$ and $A(r_2)$ from one event is

$$\frac{A(r_1)}{A(r_2)} = \frac{A_0 D(r_1)}{A_0 D(r_2)} \exp\left[-\frac{\omega}{2CQ}(r_1 - r_2)\right] \frac{I(r_1)}{I(r_2)},$$

which is related to the ratio between $I(r_1)$ and $I(r_2)$. Let $A_i(r_{ij})$ be the spectral amplitude of event i at station r_{ij} ($i, j = 1, 2$). The spectral amplitude ratio can be written as

$$\frac{A_1(r_{1j})}{A_2(r_{2j})} = \frac{A_{10} D(r_{1j})}{A_{20} D(r_{2j})} \exp\left[-\frac{\omega}{2CQ}(r_{1j} - r_{2j})\right],$$

which is independent of the station and instrument response. When seismic records excited by two events are recorded at two stations, we have

$$Q = \frac{\omega}{2C} \times (r_{12} + r_{21} - r_{11} - r_{22}) / \ln \left[\frac{A_1(r_{11})A_2(r_{22})D(r_{12})D(r_{21})}{A_1(r_{12})A_2(r_{21})D(r_{11})D(r_{22})} \right].$$

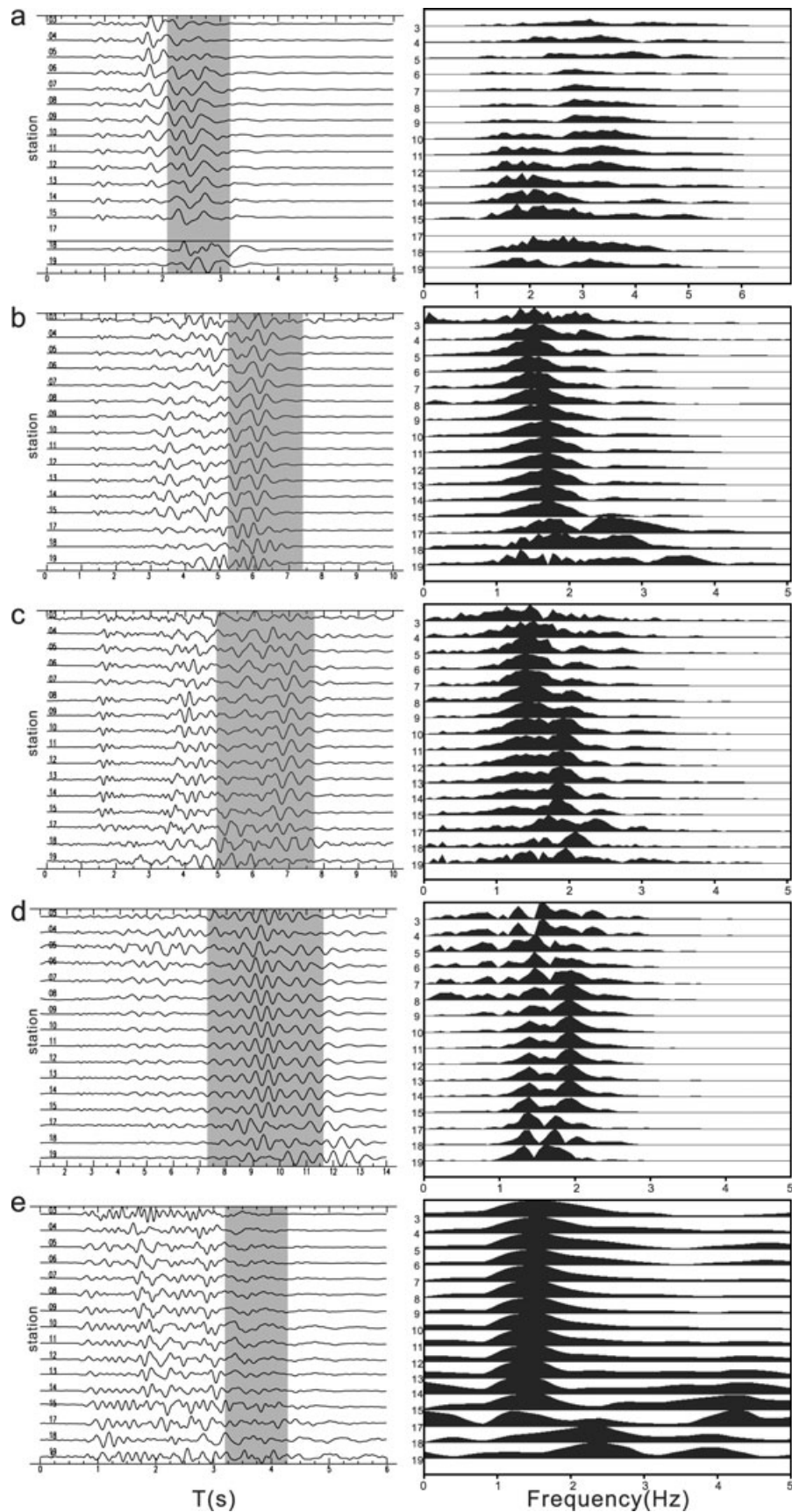


Figure 5. Coda-normalized amplitude spectra of vertical-component records along Line *B* from shots (a) SP2, (b) SP3, (c) SP4, (d) SP5 and (e) SP1. The seismograms and relevant amplitude spectra at stations on Line *B* are plotted with even trace interval. Spectral amplitudes are expressed by global normalization. Grey rectangle denotes the area of spectral analysis on the record sections. Amplitude spectra from shot SP1 are different from shots SP2 to SP5.

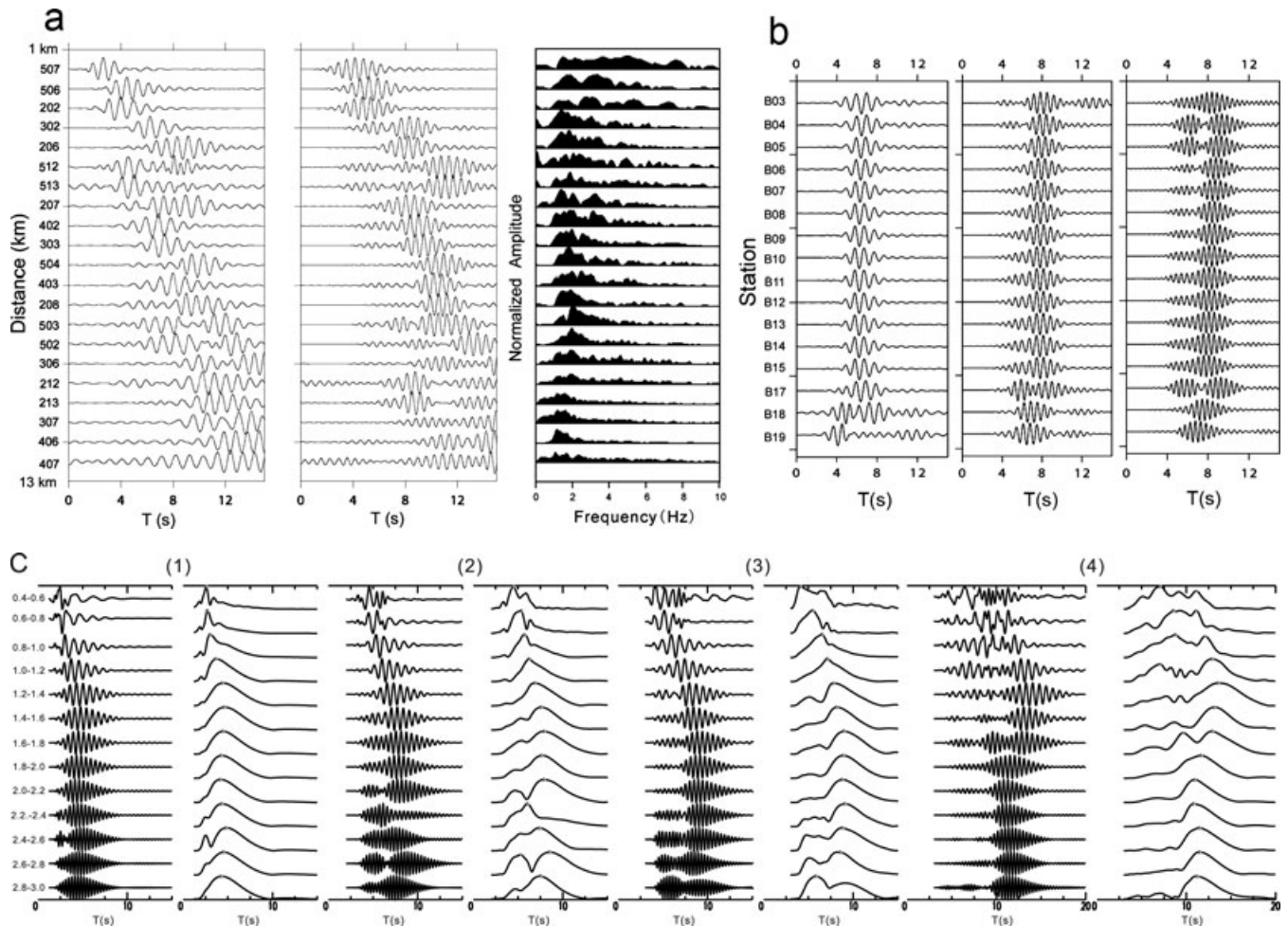


Figure 6. (a) Trace-normalized vertical-component record sections for trapped waves filtered with lower frequency bands of 0.8–1.0 Hz (left-hand panel) and 1.4–1.6 Hz (central panel) and relevant coda-normalized amplitude spectra (right-hand panel) along Line *A*. (b) Trace-normalized record sections (along Line *B*) filtered with frequency bands of 0.8–1.1 Hz (left-hand panel), 1.1–1.4 Hz (central panel) and 1.4–1.7 Hz (right-hand panel) from shot SP3. (c) Multiple bandpass-filtered seismograms and their calculated envelopes at a station (A03) within the fault zone from (1) SP2, (2) SP3, (3) SP4 and (4) SP5. The seismograms were filtered using a bandpass filter with a bandwidth of 0.2 Hz and the central frequency ranges from 0.5 to 2.9 Hz in increment of 0.2 Hz. Filtered seismograms and envelopes are plotted using channel normalization. The peaks of envelopes are denoted by solid circles.

As mentioned above, the spectral peaks of the trapped waves are at about 2.0 Hz, and the frequency range of body waves is from 4 to 10 Hz. In this estimate, Q value was calculated at six frequencies from 1 to 6 Hz. The geometric attenuation factor $D(L) = 1/\sqrt{L}$ for 1, 2 and 3 Hz for trapped waves, where L is shot-receiver distance, and $D(L) = 1/L$ for 4, 5 and 6 Hz for body waves, where L is the ray path length of the refraction waves.

In the measurement of Q , the multiple source-station pairs remove the effect of source, instrument and site effects at stations. In the KLFZ experiment, eight groups of two event-two station pair with high-quality data were formed (Table 3), where shot and station locations are shown in Fig. 1(b). In each group, quality factor Q was calculated at frequencies from 1 to 6 Hz, respectively. The mean value and the standard deviation of quality factor Q were calculated from the results of eight groups (Table 4).

The spectral amplitudes at stations on Line *A* from the shots close to the fault trace were used to calculate Q value in the fault zone. Correspondingly, the spectral ratio method was also used to estimate Q value outside the fault zone, where the stations are B03 and B05 on Line *B* and the events are SP1 and another chosen from

either SP3 or SP5 (Table 3). The final Q value within and outside the fault zone at a specific frequency is an arithmetic mean of Q measurements (Fig. 8), respectively. The uncertainty of Q estimation in the surrounding rocks is greater than that within the fault zone due to a few available records.

4 SIMULATION OF FAULT-ZONE TRAPPED WAVES

4.1 Simulation method and algorithm

The finite difference method was used to simulate the wavefield, whereby the seismic waves propagate in a 3-D medium with a planar free-surface boundary and spatially variable anelasticity (i.e. the quality factor Q). The model consists of a layered model with a low-velocity and low- Q zone sandwiched between two-layered half-spaces with relatively high-velocities and high- Q values.

Parameters used in the staggered-grid finite-difference algorithm (Graves 1996) to calculate the synthetic waveforms are as follows: a grid interval of 25 m, time step length of 0.002 s and 7500 calculation steps. The source is an explosion with a delta source function

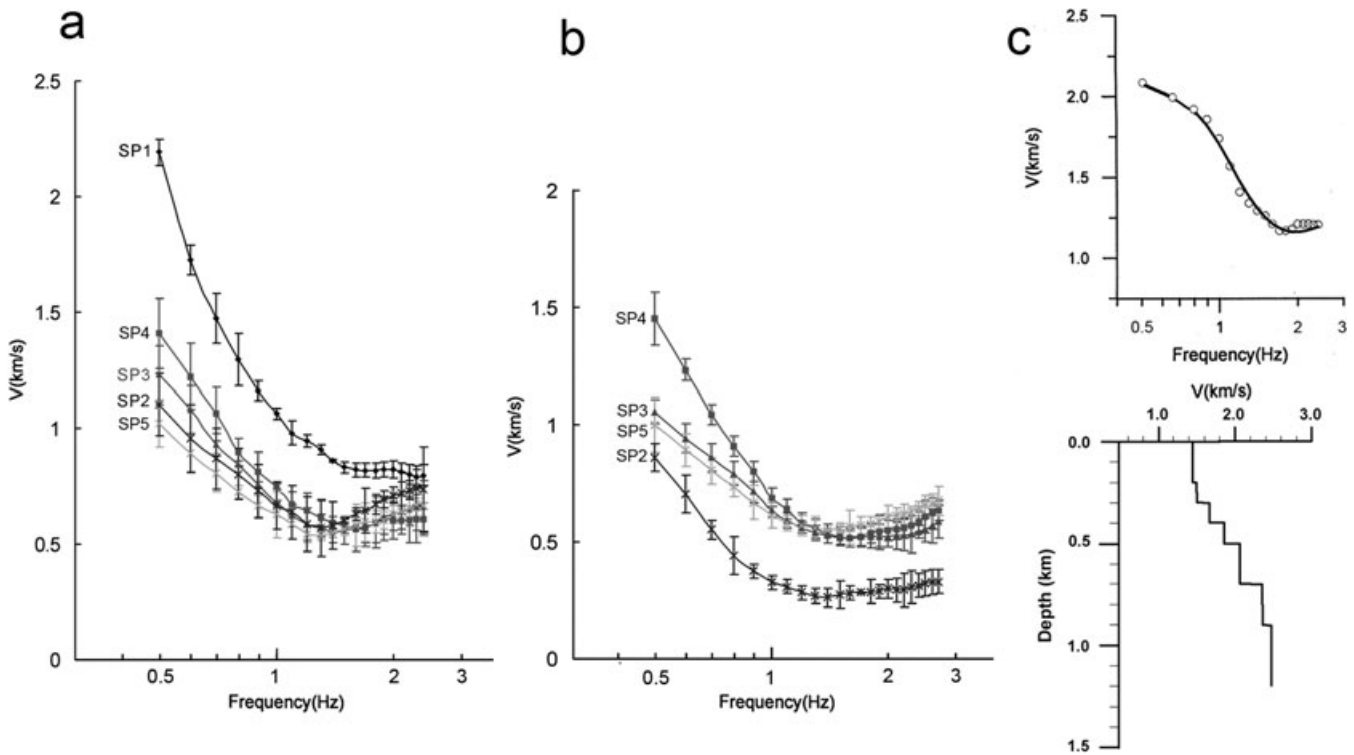


Figure 7. (a) Group velocities of trapped waves measured from multiple bandpass-filtered records along the fault-zone profile (Line *A*) for shots SP1 to SP5. Each data point denotes an average of the group velocities measured at all stations along the fault zone at the specified frequency. The standard deviation is denoted by error bar at each point (frequency, velocity). The group velocities from shot SP1 outside the fault zone are higher than those within the fault zone. (b) Group velocities of trapped waves measured from multiple bandpass-filtered records cross the fault zone (Line *B*) for shots SP2 to SP5. Each point denotes an average of the group velocities measured at eight stations close by the rupture trace on Line *B* at the specified frequency. (c) Fitness of the calculated group velocities to the observation shown in Fig. 7(a) and the relevant *S*-wave velocity models from shot SP1. Top panel: measured (circles) and calculated (thick line) group velocities. Bottom panel: 1-D *S*-wave velocity structure.

Table 3. Pairs of two events and two stations.

Area	Group	Event 1	Event 2	Station 1	Station 2
Fault zone	1	SP2	SP5	A02	A06
	2	SP2	SP5	A03	A07
	3	SP3	SP5	A02	A06
	4	SP3	SP5	A02	A07
	5	SP3	SP5	A03	A06
	6	SP3	SP5	A03	A07
Surrounding rocks	7	SP1	SP3	B03	B05
	8	SP1	SP5	B03	B05

and a rise time of 0.1 s. A four-pole Butterworth filter with a low cut-off at 0.2 Hz and a high cut-off at 6.0 Hz was used at the source. The gridpoint number in the 3-D model is 100 (*x*) × 380 (*y*) × 200 (*z*), where the *x*-axis is perpendicular to *y*, the *y*-axis is parallel

to the rupture trace and the *z*-axis is depth. The total number of gridpoints is 7.6×10^6 . The fault zone is depicted as a low-velocity zone along the central part of the grid network. A point source is embedded within the fault zone at a depth of 25 m. Station B10 is located at the central line of the low-velocity zone, which coincides with the rupture trace. Supposing the fault-zone width of 300 m, stations B06 and B15 on Line *B* are, respectively, located on the two-side boundaries of the fault zone.

4.2 Effects of fault-zone width on wavefield

As presented by Ben-Zion & Aki (1990) and Igel *et al.* (1997), the waveform character of fault-zone trapped waves is related to the fault-zone width. In the KLFZ experiment, the vertical-component record sections of shots SP3–SP5 show that the waveforms of trapped waves at 10 stations close to the rupture trace (from B06

Table 4. Quality factor *Q* within and outside the fault zone.

Frequency (Hz)	Group 1	Group 2	Group 3	Group 4	Group 5	Group 6	Group 7	Group 8	Mean <i>Q</i> Value	
									In	Out
1	11	12	10	13	10	14	19	25	11	22
2	15	16	14	16	13	11	33	22	14	27
3	19	18	18	13	20	15	23	33	17	28
4	16	19	20	25	21	19	26	38	20	32
5	30	26	23	28	24	25	35	49	26	42
6	33	28	30	30	31	29	45	55	30	50

‘In’ is the fault zone and ‘Out’ is the surrounding rocks.

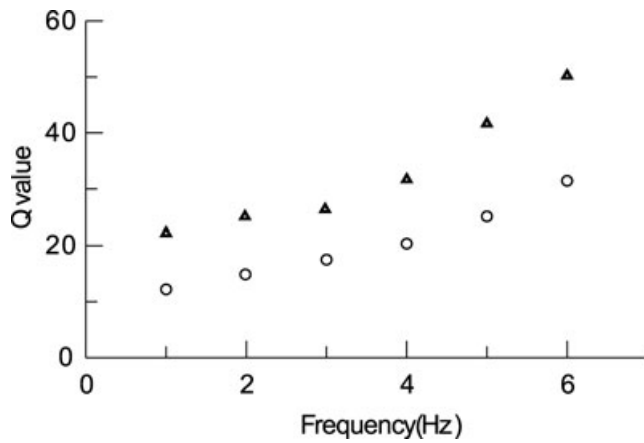


Figure 8. Mean Q values at six frequencies within the fault zone (circles) and the surrounding rocks (solid triangles).

to B15) do not bear significant differences (Figs 4b–d). In addition, the amplitude spectra at stations from B06 to B15 for shots SP3 to SP5 show good consistency (Fig. 5).

In order to understand the effects of the fault-zone width, we set up a simplified model (Fig. 9a, top panel) with different fault-zone widths (200, 300 and 400 m). To simulate the record section of shot SP4 on Line *B* (Fig. 4c), the synthetic seismograms were calculated on the simplified models at distance of 5.5 km from source to

Line *B* (Fig. 9a, bottom panel). A low-velocity zone with a smaller width (200 m) generates higher frequency trapped waves than that with larger width (300 and 400 m). The trapped waves generated by waveguide with a width of 300 m give a better fitness to the record section. According to the analysis of the seismic wavefield, the energy of trapped waves in the low-velocity zone could pass through the boundary of the zone and propagate in the surrounding rocks to a certain extent. Different frequency bands on seismic records may define the width of the damage zone (e.g. Peng *et al.* 2003; Peng & Ben-Zion 2004).

4.3 Effect of velocity contrast on wavefield

The velocity contrast between the low-velocity fault zone and the surrounding rocks has significant effect on wavefield. For this simulation, the calculation of synthetic seismograms was based on the simplified model with different velocity contrast. Fig. 9(b) shows that the lower velocity contrast causes the trapped waves to propagate outwards farther extent from the boundary than that by the higher velocity contrast. Considering the precise extent of the trapped waves on the record sections on Line *B* (Fig. 4), the locations of the south and north boundaries of the low-velocity zone can be identified as being between stations B05 and B06, and between B15 and B17, respectively. However, there is a large gap (~70 m) between stations B05 and B06 and an even larger gap (~80 m) between stations B15 and B17. Therefore, the boundary location of the low-velocity zone has a certain error.

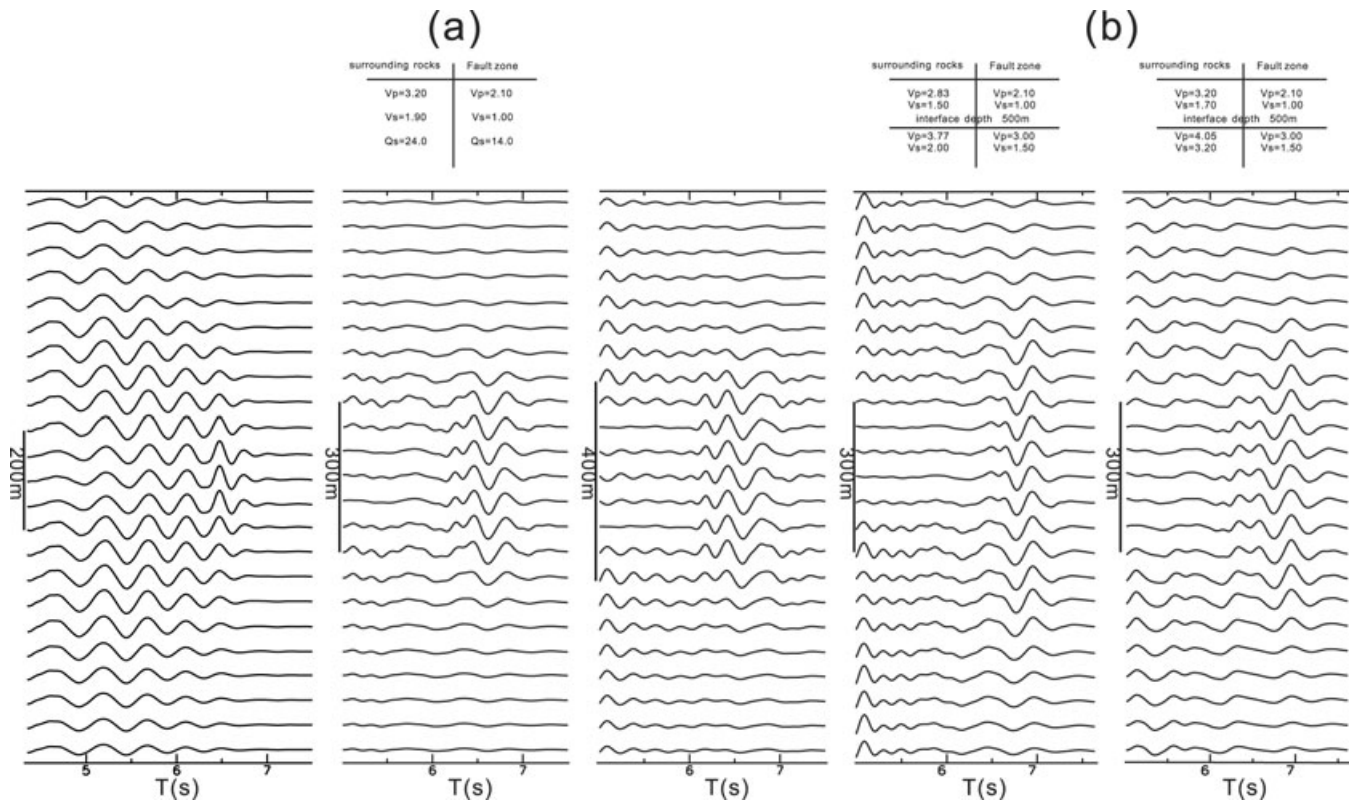


Figure 9. (a) Vertical-component synthetic seismograms of trapped waves based on different fault-zone width. The fault-zone model consists of a low-velocity zone with surrounding rocks. Upper panel: velocity model and lower panel: three synthetic sections calculated at distance of 5.5 km on the models with fault-zone width of 200, 300 and 400 m, respectively. (b) Synthetic seismograms of trapped waves with different velocity contrast between surrounding rocks and low-velocity zone. Upper panel: velocity models and lower panel: vertical-component synthetic sections at distance of 5.5 km on the models with fault-zone width of 300 m. All of the synthetic seismograms were filtered with low passband (<3 Hz) and plotted with trace normalization and station interval of 50 m. Velocity unit: km s^{-1} .

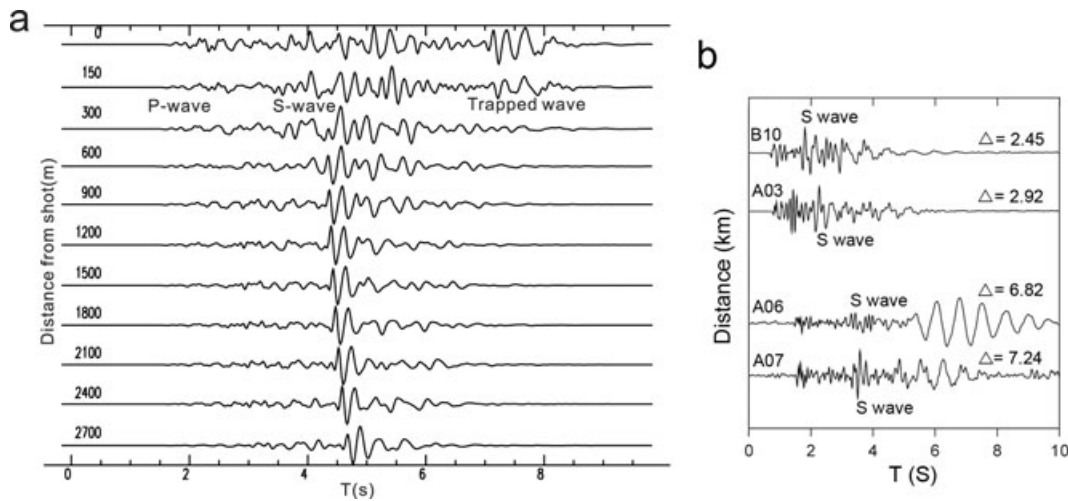


Figure 10. (a) Trace-normalized synthetic seismograms calculated on the three-layer fault-zone model in Table 5. Receiver is located on the central line of fault zone, and at a distance of 7 km from station B10 on Line B. The source is an explosion located on Line B (see Fig. 11). The number on the trace denotes the distance from the source to station B10 on Line B. The trapped wave energy obviously decays with distance from source to the central line of fault zone. (b) Trace-normalized vertical-component seismograms recorded at four stations which are close to the rupture trace of KLFZ. Source is shot SP1.

4.4 Wavefield excited by shots outside fault zone

Some studies (e.g. Li *et al.* 1994) presented that the trapped waves of fault zone are only generated when the sources are close to or inside the low-velocity fault zone. In addition, the trapped waves from sources outside fault were numerically simulated by Fohrmann *et al.* (2004), where considerable trapping efficiency is possible for source well outside a shallow fault zone, and large source volumes are able to generate local amplification above faults. The observation above the Karadere–Düzce branch of the North Anatolian fault has shown that trapped wave energy is generated by earthquakes occurring in a large volume around the active fault (Ben-Zion *et al.* 2003).

To simulate the trapping efficiency excited by a point source outside the fault zone, we calculated synthetic seismograms on a three-layer fault-zone model. Fig. 10(a) shows the energy decay of trapped waves with distances from shot to the fault zone. An explosion generates significant trapped wave energy when the distance from source to the fault zone is smaller than about 600 m. The energy decay is faster than that generated by the source of large volumes in Fohrmann *et al.* (2004). Fig. 10(b) shows the vertical-component seismograms at four stations close to the rupture trace, excited by shot SP1. Though the oscillatory shear wave trains after the S arrival in the records at station within the fault zone are evident, the energy ratio between trapped waves and S waves from the sources outside the fault zone is smaller than 1.0, which is consistent with that of synthetics in Fig. 10(a), except for the record at station A06, where there exists abnormal low-frequency response on vertical component. It is probably caused by the local site effect.

4.5 Quantitative analysis of fitness between synthetics and observation

The initial 3-D velocity model was formed from several sources, including the 1-D velocity model along the fault zone (Table 2), the inversion of surface-wave group velocities (Fig. 7c), the apparent velocities of phases P2 and S2 (Figs 3a and b) and the Q estimation (Table 4). Fig. 11 shows a three-media model of KLFZ, with three layers, fault zone, source and receivers on Line B. Actually, the 3-D model in this paper should be a $2\frac{1}{2}$ -D model, or called pseudo-3-

D model. A forward modelling approach was used to model the observed waveforms. Due to the limited observed data, the number of model parameters is decreased in the numerical simulation, that is, we only make a trade-off between the fault-zone width and quality factor Q , which are primary parameters to affect the waveform of the trapped waves, and fix other parameters on the model.

In order to quantitatively analyse the fitness between synthetics and observed trapped waves, we calculated the correlation coefficients of synthetic and observed waveforms. A 2-D grid search process was carried out in an appropriate range of the fault-zone width and quality factor Q , where the fault-zone width is from 125 to 475 m with step of 25 m, and the quality factor Q is from 5 to 50 with step of 5. Fig. 12(a) shows the topography of correlation coefficients of the trapped waves between synthetics and observed records from shots SP3 and SP4. The correlation coefficient has the maximum value of 0.76 for a fault-zone width of 300 m and a quality factor Q of 15. Figs 12(b) and (c) show the cross-section of correlation coefficients at the Q value of 15 and at the fault-zone width of 300, respectively. The topography illustrates that the maximum value of the correlation coefficients is global, and so the determination of the fault-zone width and quality factor Q is reasonable.

4.6 Final KLFZ model

The final KLFZ model (Table 5) shows a three-layer 3-D velocity structure. Shear velocities in the fault zone are 30–45 per cent smaller than that in the surrounding rocks from the surface to a minimum depth of 1 km. The synthetic seismogram sections along Line A and Line B (Figs 13 and 14) were, respectively, calculated on the final 3-D KLFZ model. The dispersive behaviour of the trapped waves after the S arrival is evident. On the trace-normalized vertical-component synthetic sections, the amplitude of the first P arrival is smaller than that of the trapped waves, but still clear. Although the traveltimes between synthetics and observations along the fault zone are quite consistent, the fitting of the amplitude is more variable, reflecting simplicity of our 3-D anelastic model.

Figs 15(a) and (b) show the fitness of the vertical- and radial-component synthetics with observations on Line B for shots SP3 and SP4, respectively, where a low pass filter with cut-off frequency

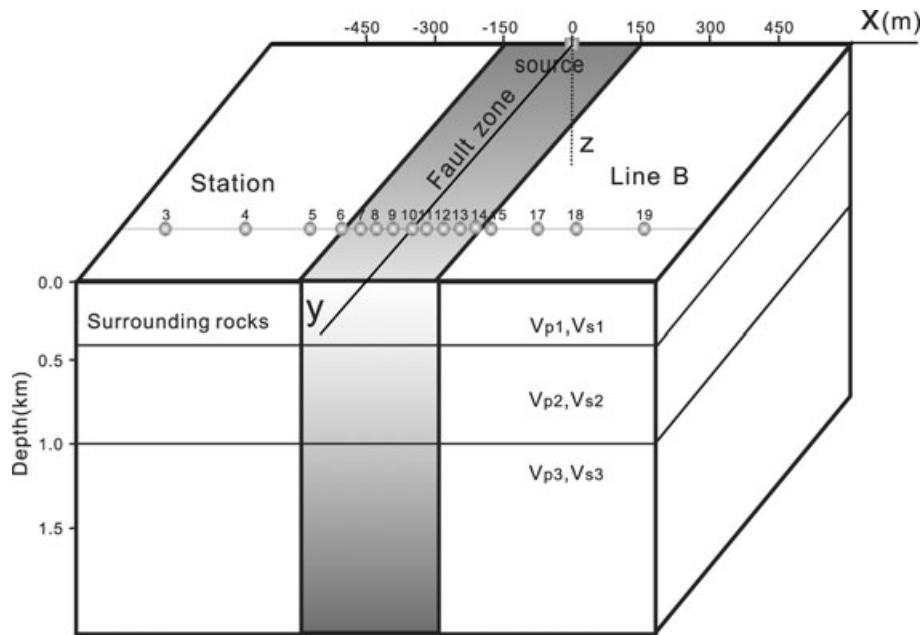


Figure 11. Stereoscopic diagram of KLFZ, illustrating the three-media fault-zone model for a laterally heterogeneous low-velocity fault-zone structure, with an example of source location and seismic recording stations (Line B).

of 6.0 Hz was used. The synthetic trapped waves for stations B06 to B15 are consistent with observations on both vertical and radial components. Figs 16(a) and (b) show the fitness of synthetic and observed waveforms and amplitude envelopes at station B10 for shots SP3 and SP4 in the frequency band from 0.5 to 2.3 Hz, respectively. For shot SP3, the correlation coefficients calculated in the time interval from 5 to 10 s are from 0.643 to 0.862, where the maximum value (0.928) falls into the frequency band 1.7–2.0 Hz. For shot SP4, the correlation coefficients in the time interval from 5 to 10 s are from 0.520 to 0.927. The maximum value (0.987) also falls into the same frequency band as that for SP3. The relevant amplitude envelopes at station B10 (Figs 16a and b, bottom) show that the synthetic and observed amplitude envelopes have a fair fitness of above 0.8 Hz.

5 DISCUSSIONS

5.1 Physical properties of shallow fault zone

The results concerning physical properties of the damage zone of Kunlun fault are highly consistent with the studies of other major strike-slip faults, such as the San Andreas Fault, where the damage zone is 150-m wide, and it has a *S*-wave velocity reduction of 30–40 per cent and a quality factor *Q* of 10–50 (Li *et al.* 2004). These results are consistent with earlier studies by Lees & Malin (1990), Michelini & McEvilly (1991) and Thurber *et al.* (1997), and the study of San Jacinto fault by Lewis *et al.* (2005). Many of our insights regarding the properties of the shallow KLFZ are based on the characteristics of the fault-zone trapped waves and quantitative analysis of these waves. Due to the dispersion feature, the position of the centre point of trapped waves changes with frequency (Figs 16a and b). Fig. 13 illustrates that the time differences between the *S* arrival and the trapped wave group increase with shot-receiver distance along the fault zone. Shear velocities in the fault zone are reduced by 30–45 per cent smaller than those in the surrounding rocks from the surface to a depth of at least 1 km.

The numerical simulation of trapped waves excited by explosive sources near the surface demonstrates that the trapped waves propagate from the surface to about 1–2 km in depth. Phases P3 and S3 are clear at distances from 3.5 to 15.0 km, and are considered as refractions from the interface at the depth of about 1 km on the basis of the record sections along Line A (Figs 2a and b). The essential prerequisite for generating these refractions is that the medium below the interface is vertically homogeneous for head waves, and the layer has a definite thickness. Thus, the *S*-wave velocity reduction extends to the depth below 1 km.

Recent observations suggest that the fault-zone trapped waves can be produced in fault zones that are not currently active (e.g. Rovelli *et al.* 2002). Fault-zone waveguide structures could be a common feature, and related to the top part of a flower-type structure within the fault zone that is highly damaged and usually aseismic (Ben-Zion *et al.* 2003). As mentioned above, KLFZ is a long-lived palaeo-earthquake fault zone, which may have experienced hundreds of earthquakes, with an evident width in the surface geology. Based on recent studies, we have not found any evidence that the recent rupture trace was generated by previous earthquakes, and we have no way to distinguish the relative roles in creating the waveguide effects by recent and previous earthquakes. Therefore, the shallow structure of KLFZ imaged in this paper is in response to the cumulative effects of earthquakes in the past, though the authors consider the pronounced waveguide structure (i.e. 30–45 per cent *S*-wave velocity reduction) to be possibly an effect enhanced by the recent rupture.

5.2 Head waves on the records along line A

The first *P* arrival P3 (head wave) beyond the critical distance of 3.65 km in Fig. 2(a) has an apparent velocity of 5.35 km s⁻¹. It would have been equal to the velocity of the faster medium if the phase were a ‘head wave’ refracted along the cross-fault material contrast, as discussed by Ben-Zion & Malin (1991), who analysed microearthquake seismograms from a borehole seismic network,

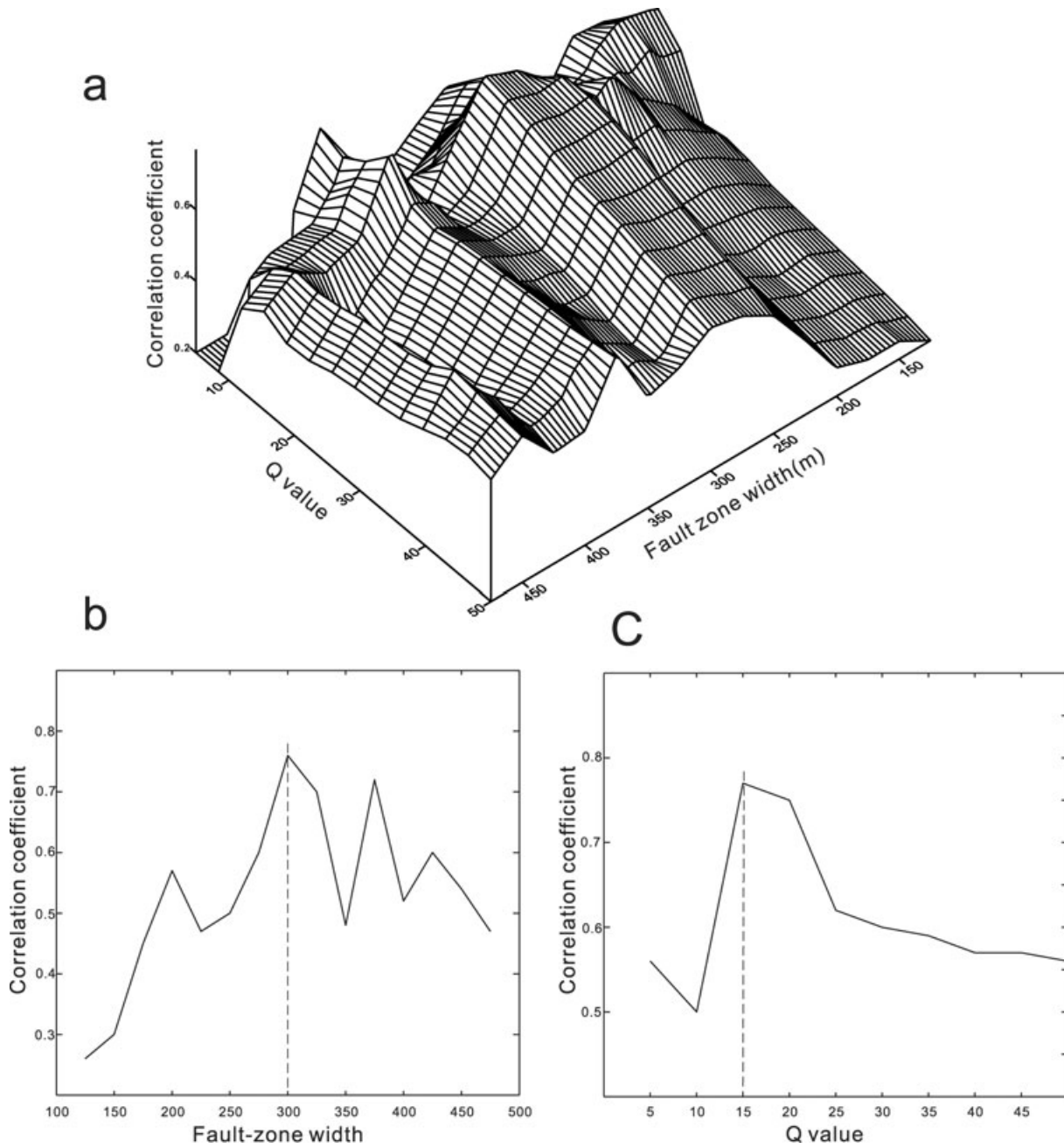


Figure 12. (a) Topography of correlation coefficients of the trapped waves between synthetic and observed waveforms from shots SP3 and SP4 on a 2-D area of fault-zone width and Q value, where the fault-zone width is from 125 to 475 m with step of 25 m, and Q value is from 5 to 50 with step of 5. (b) Cross-section of correlation coefficients at Q value of 15. The maximum value is located at fault-zone width of 300. (c) Cross-section of correlation coefficients at fault-zone width of 300.

Table 5. Final 3-D fault-zone velocity model.

Layer No.	Waveguide width (m)	Thickness of layer (km)	V_p (km s ⁻¹)		V_s (km s ⁻¹)		ρ (g cm ⁻³)		Q	
			In	Out	In	Out	In	Out	In	Out
1	300	0.40	2.3	3.3	1.0	1.9	1.7	1.9	15	35
2	300	0.65	4.0	4.4	1.9	2.9	2.2	2.4	15	35
3	300	*	5.4	5.8	2.6	3.5	2.6	2.9	15	35

'In' is the fault zone and 'Out' is the surrounding rocks. Asterisk denotes semi-infinite layer.

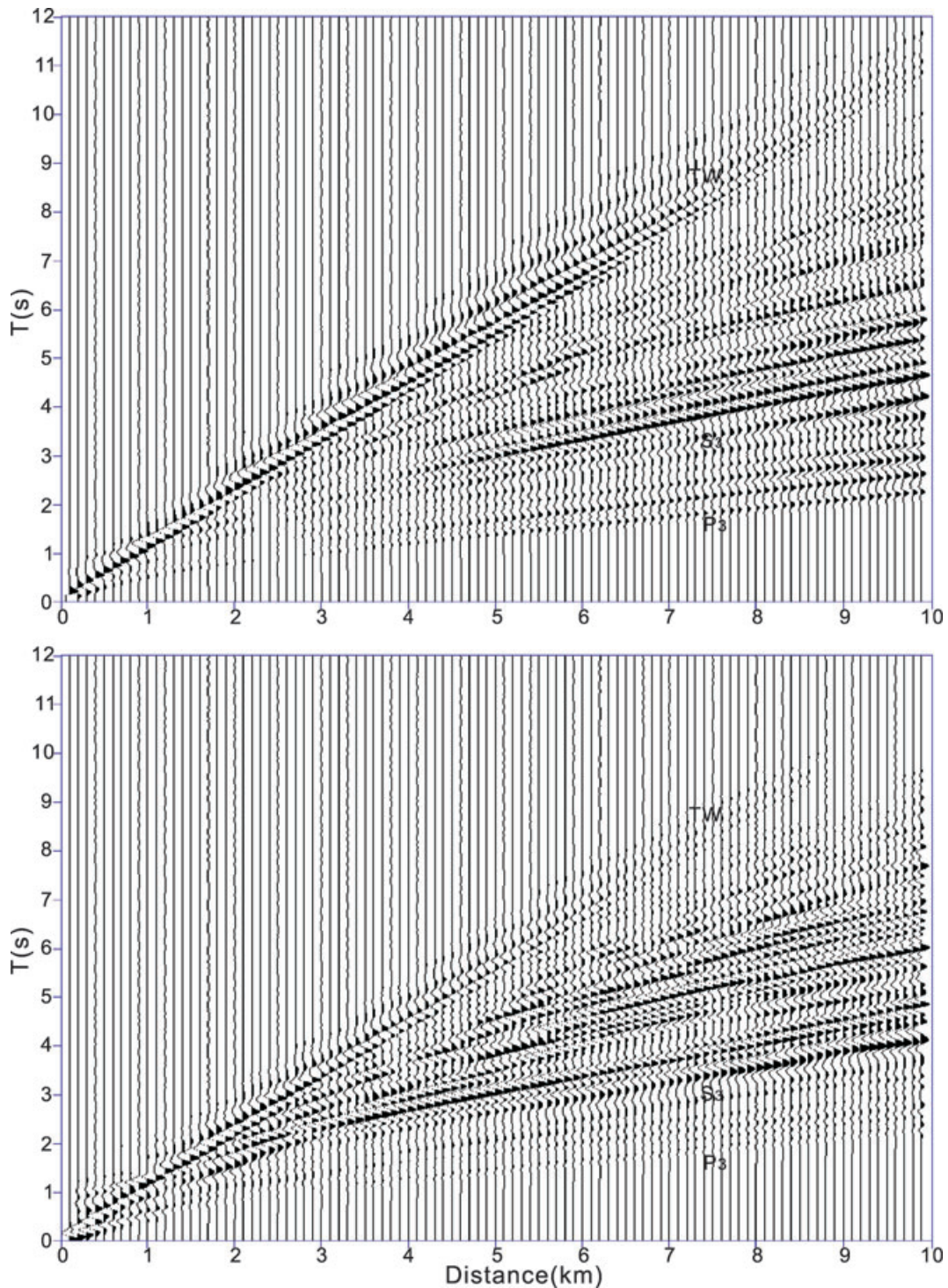


Figure 13. Synthetic seismograms recorded on Line *A*. The time differences between the *S* arrival and the trapped wave group increase with distance along the fault zone. Trace interval is 100 m. Top panel: vertical component and bottom panel: radial component. *Tw*: Trapped waves; *P3* and *S3*: refractions same as in Figs 2(a) and (b).

where the focal depths are about 5 km. In general, source depth is critical for judging the existence of head wave arrivals. In the KLFZ experiment, both sources and receivers are located at the surface. The surrounding rocks would have had a high velocity (5.35 km s^{-1}) near the surface if the phase *P3* were refracted along the cross-fault material contrast. *P*-wave velocity inside the fault zone in a shallow layer is determined to be 2.25 km s^{-1} by the arrival times of phase

P1 (direct wave) (see Fig. 17a). Phase *P3* has an intercept time of 0.34 s and an arrival time of 1.15 s at the distance of 4.30 km on trace 302 (Fig. 2a).

Fig. 17(b) illustrates the possible paths of head waves and the related traveltime curve when the head waves are generated along the cross-fault material contrast. Based on the velocities of the faster and slower media and the intercept time, the half-width of fault zone

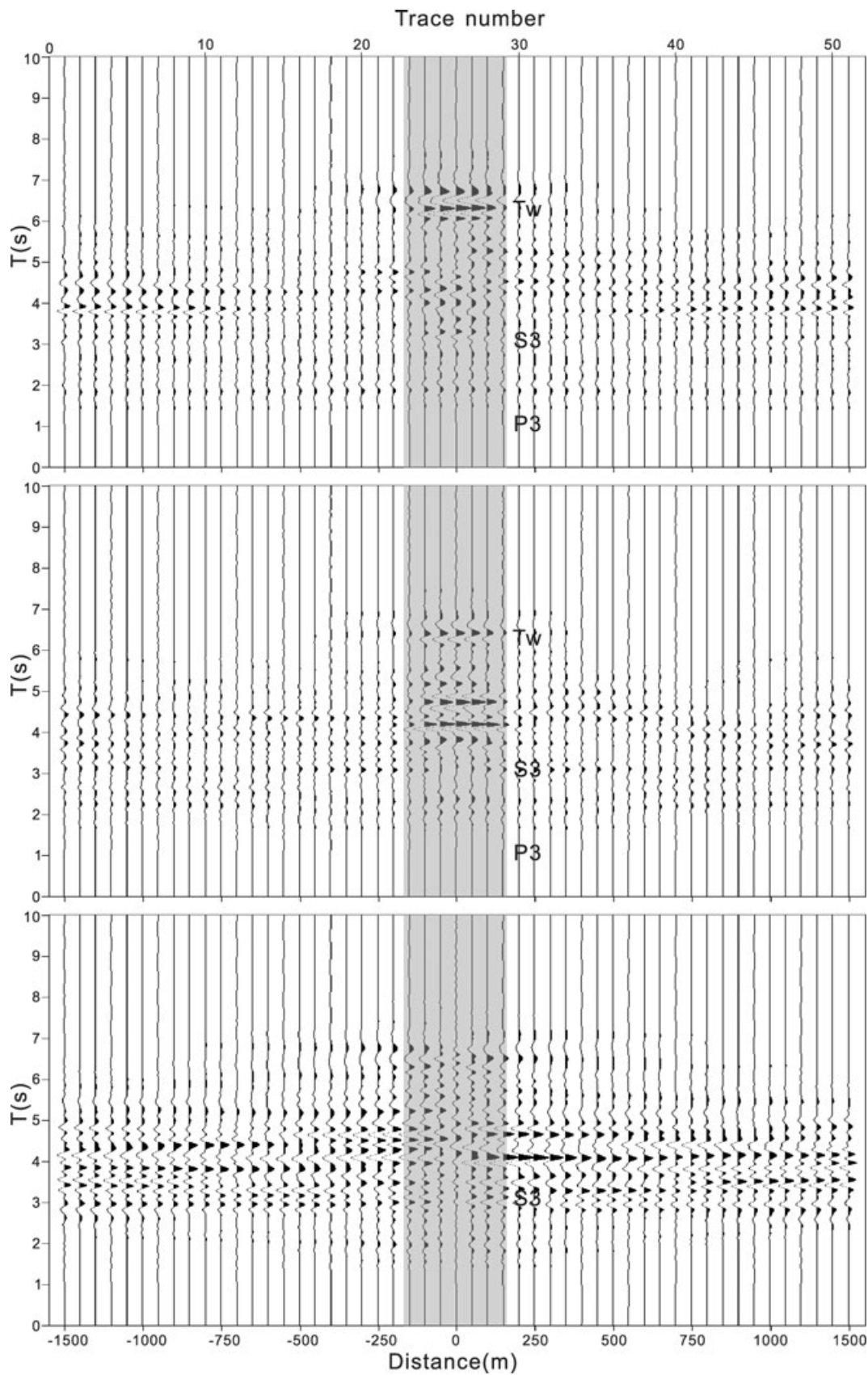


Figure 14. Synthetic seismograms from shot SP4, recorded on Line B. Trace interval is 50 m. Top panel: vertical component, middle panel: radial component and bottom panel: transverse component. *Tw*: Trapped waves; P3 and S3: refractions same as in Figs 4a and (b).

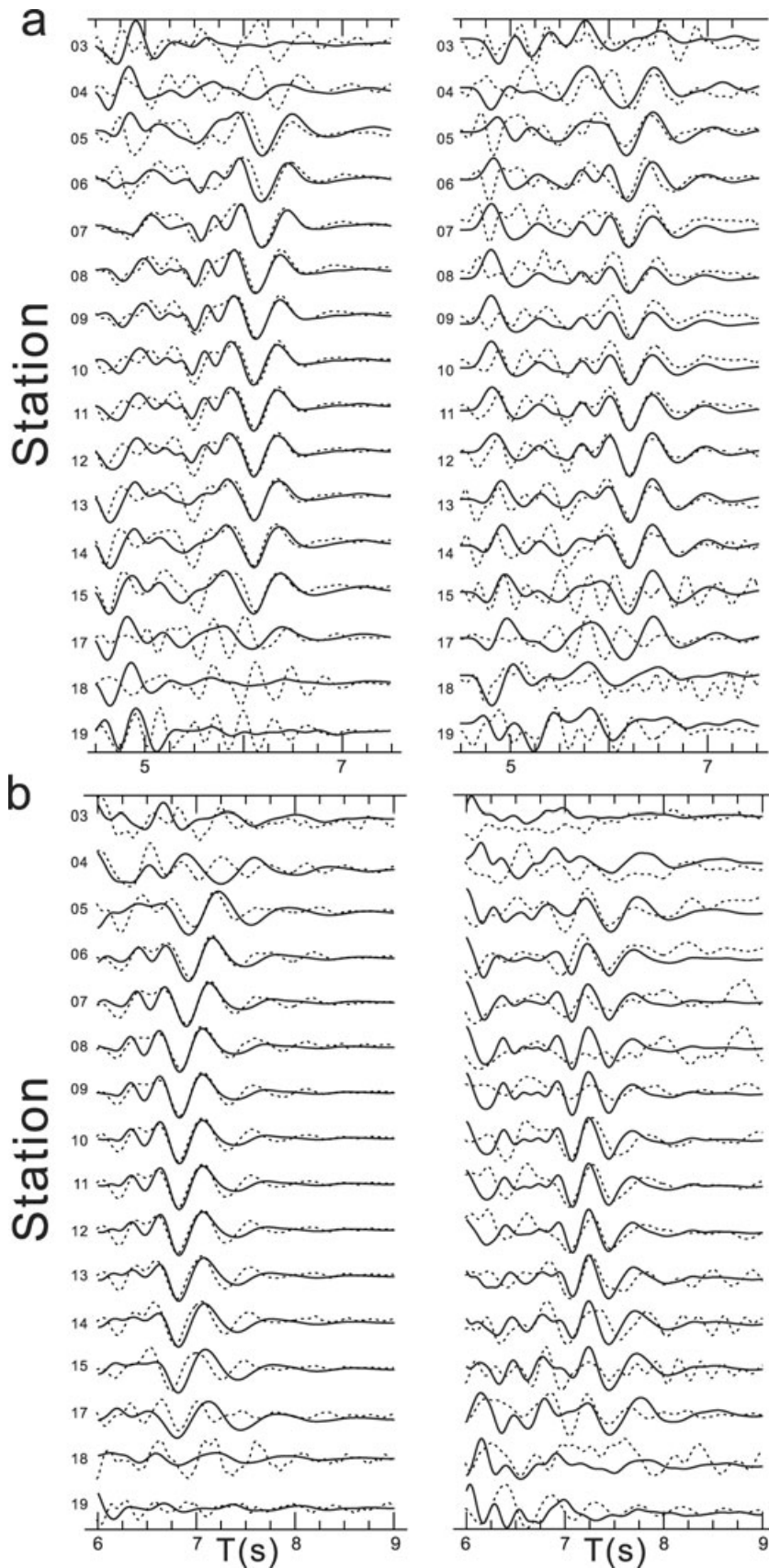


Figure 15. Comparison of trapped waves on vertical- and radial-component synthetics (solid lines) with observations (dotted lines) on Line *B* for shots (a) SP3 and (b) SP4. A low-pass filter with cut-off frequency of 6.0 Hz was used to filter both synthetics and observations. Left-hand panel: vertical component and right-hand panel: radial component.

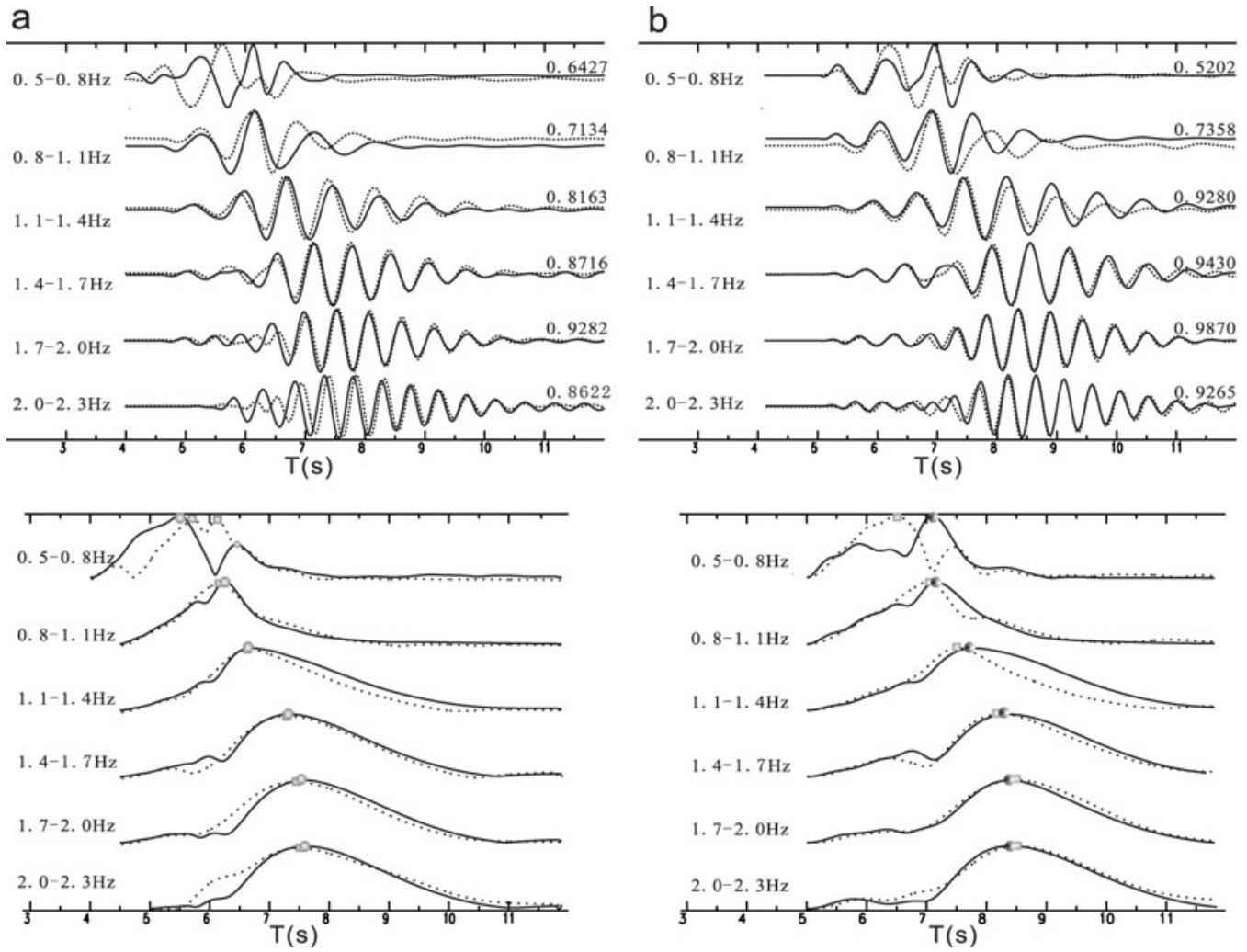


Figure 16. Comparison of synthetics and relevant amplitude envelopes (solid lines) with observation (dotted lines) at station B10 in frequency band from 0.5 to 2.3 Hz. (a) Shot SP3; (b) shot SP4; top panel: waveform fitting and bottom panel: amplitude envelope fitting.

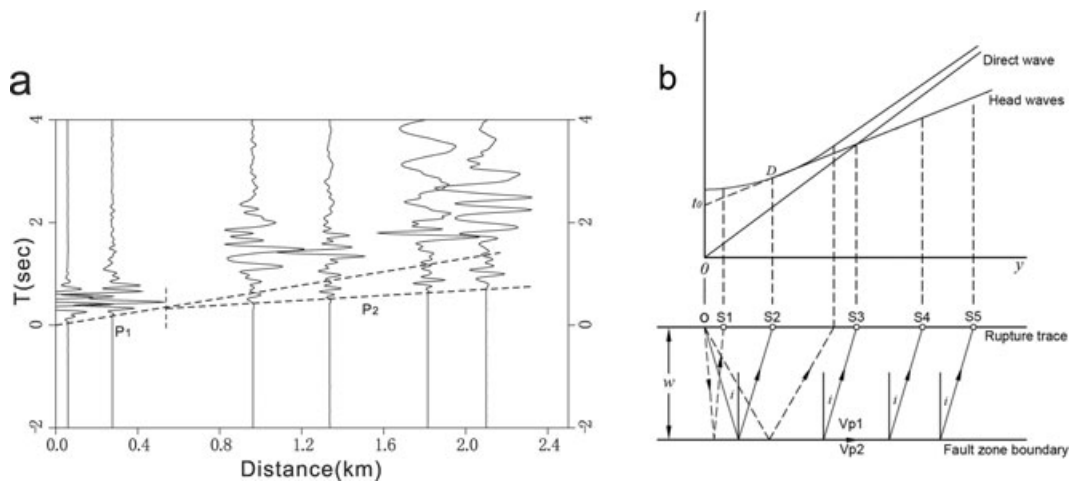


Figure 17. (a) Records at distances from 0 to 2.4 km on Line A. Phase P1 is direct wave, whose apparent velocity (2.25 km s^{-1}) is determined by arrival times. (b) Travel-time graph and ray path diagram for direct wave and head waves. Upper panel: time-distance graph of direct wave and head waves showing crossover distance at S3. Lower panel: ray paths passing through the fault zone. 'W' denotes the half of the fault-zone width, t_0 is the intercept time.

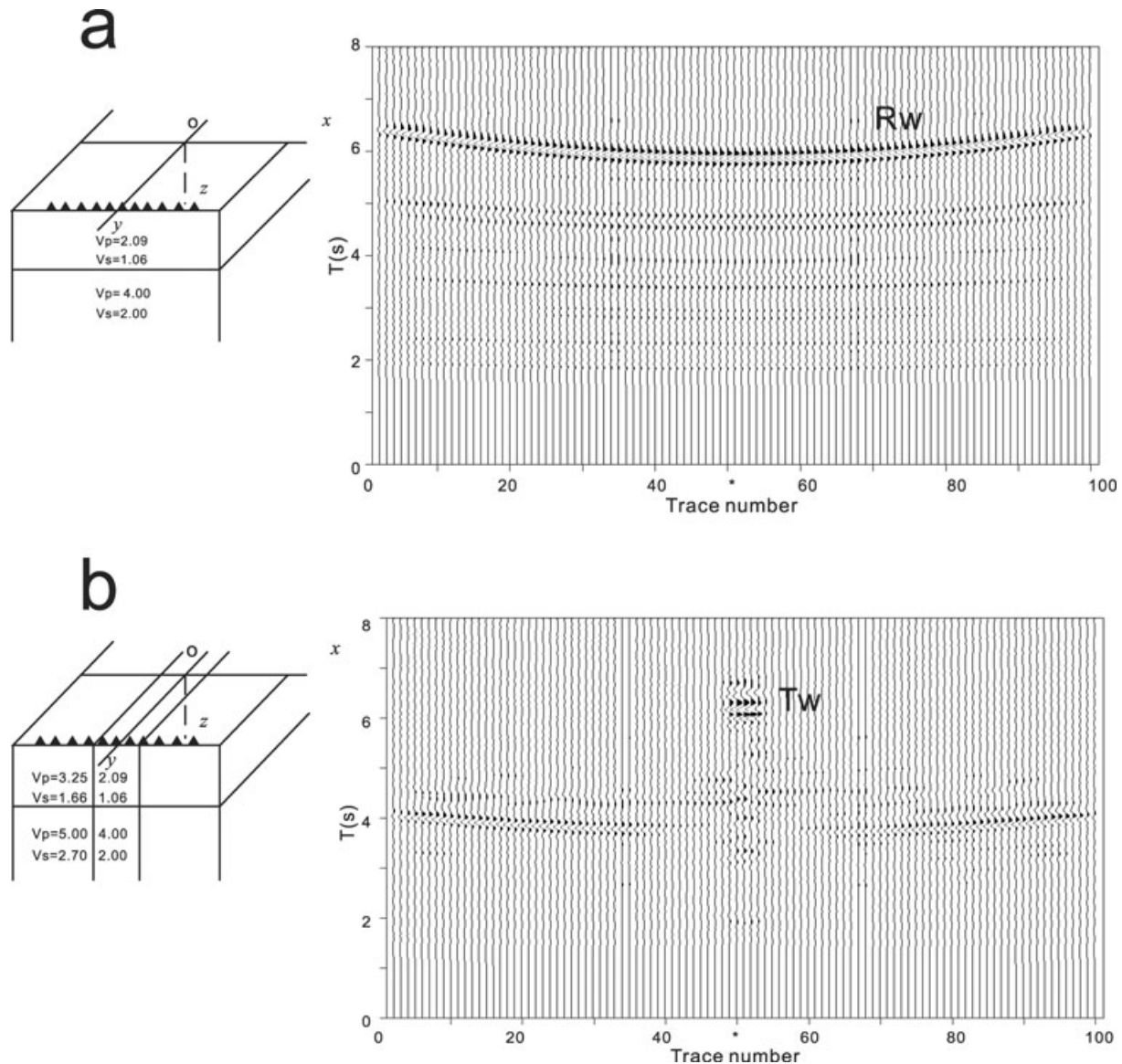


Figure 18. Synthetic seismograms excited by an explosion on two models (left-hand panel) and particle motions on the (y, z) plane from observed records. Distance from shot to station line (triangles) is 5.5 km. Asterisks below the synthetic sections denote rupture trace. Trace interval is 50 m. (a) Synthetics on the model of layered medium with the near-surface low-velocity layer. ‘ R_w ’ denotes the Rayleigh waves. (b) Synthetics on the fault-zone model with a low-velocity zone and the near-surface low-velocity layer. ‘ T_w ’ denotes trapped waves. (c) Synthetics at station B10 on Line B, calculated on models of Figs 18(a) and (b), respectively. Amplitude ratio between the Rayleigh waves (R_w) and the trapped waves (T_w) is about 0.2. (d) Particle motion on the (y, z) plane (see Fig. 11) from shot SP4, plotted on records from 6 to 8 s. (e) Particle motion on the (y, z) plane from shot SP5, plotted on records from 8 to 11 s.

is determined to be 422 m using geometric ray theory. It means that the fault-zone width would be 844 m. Previous studies (Haberland *et al.* 2003; Peng *et al.* 2003; Li *et al.* 2004) presented that fault-zone width is highly variable, ranging from several tens of metres to 200–300 m. But a fault-zone width of over 800 m has not been reported for a near-vertical strike-slip fault. Furthermore, on the off-line record sections cross fault-zone boundary (Figs 4b–d), there is not obvious difference of the arrival time of phase P3 between two sides of the boundary. This explains that phase P3 does not refract from the boundary.

Reflected P wave on the free surface cannot be separated from the original P wave due to the limited depth source and on-surface stations. As mentioned in Section 3.2.1, the Earth’s free surface is a likely cause for converted P – S waves from an explosive point source (Fertig 1984). Exact shot positions and times may contribute

to determine the behaviour of seismic phases and reduce uncertainty of phase recognition. In this paper, the head waves P3 along Line A are interpreted to be the phase along a faster medium below the low-velocity layer near the surface, as is illustrated by a routine analysis in exploration seismology.

5.3 Rayleigh waves excited by explosion

Rayleigh waves are generally created by an explosion for a velocity model with a surficial low-velocity layer. The KLFZ model deduced in this paper involves not only a low-velocity zone in the fault parallel direction, but also a low-velocity zone in vertical direction. Under this circumstance, an explosion excites both trapped waves and Rayleigh waves. Synthetic seismograms were calculated for

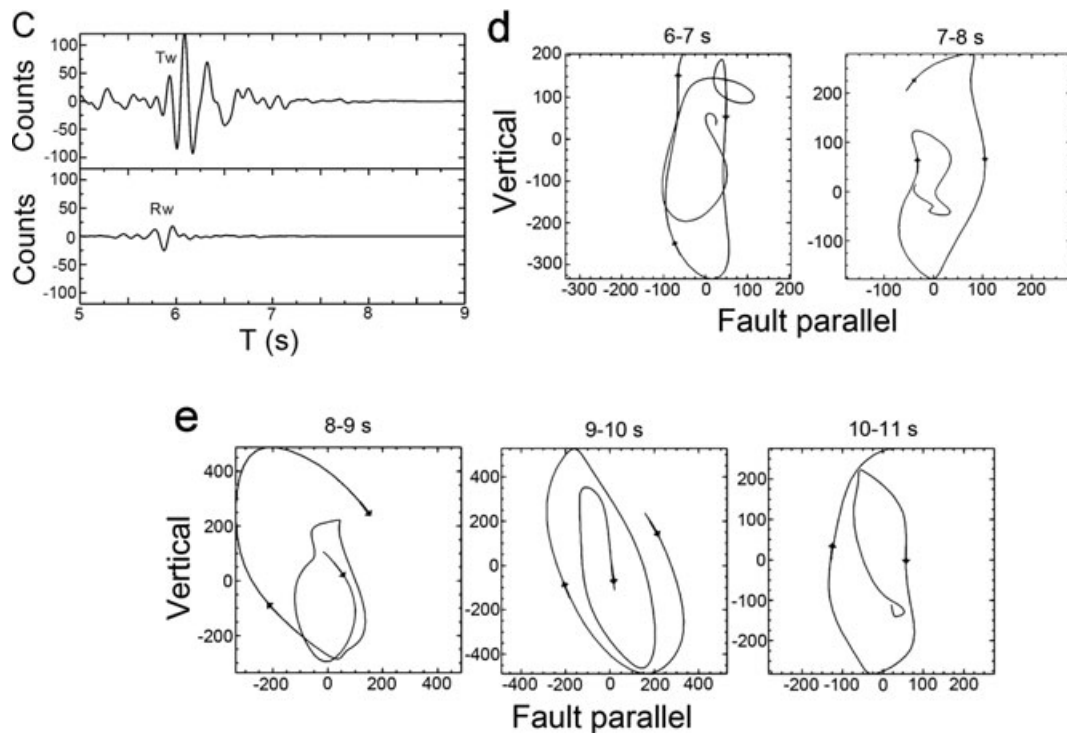


Figure 18. (continued.)

such a model by using the finite-difference algorithm. Figs 18(a) and (b), respectively, show the synthetic Rayleigh waves and trapped waves on two models with a low-velocity zone, which indicate that the amplitude of Rayleigh waves is about one-fifth of that of the trapped waves (Fig. 18c), though two kinds of surface waves present similar amplitude spectra.

Theoretically, for Rayleigh waves, the particle of the medium describes a retrograde ellipse and the maximum displacement parallel to the direction of propagation is about two-thirds of that in the vertical direction. In the KLFZ experiment, the particle motions at station B10 from the shots Sp4 and SP5 present clockwise rotation, as shown in Figs 18(d) and (e), which indicate that the main part of the arrival with a high-amplitude, low-frequency and long-wave train behind *S* arrivals should indeed be the trapped waves.

6 CONCLUSIONS

We present a shallow crustal model of the KLFZ along a segment of the fault zone that ruptured in the *M*8.1 earthquake on 2001 November 14. The seismic data involve a 15-km-long active-source seismic refraction profile and fault-zone trapped waves generated by explosive sources. The recording arrays were located both along and across the Kunlun fault. Fault-zone trapped waves were clearly recorded on the vertical and horizontal components of the seismometers.

The active-source seismic profile along the fault provides refraction measurements of *P*- and *S*-wave seismic velocities in the upper ~1–2 km of the fault zone. In comparison with the crust outside the fault zone, *S*-wave velocity at a depth of 1 km is reduced by 25 per cent and *P*-wave velocity is reduced by 12 per cent; velocity reductions are still larger at depths <1 km. Thus, the damage zone has a much larger reduction in *S*-wave velocity than in *P*-wave, an observation that is consistent with previous studies of fault-zone properties. *P*-wave velocities in the surrounding rocks are reduced

by 7–20 per cent. The fault zone with such *P*- and *S*-wave low velocities is an indication of high fluid pressure because V_s is affected more than V_p .

Quantitative analysis of the correlation coefficients of the trapped waves between synthetic and observed waveforms indicates that the KLFZ width is 300 m, and the shear-wave quality factor Q within the fault zone is 15. The physical properties of the damage zone of the Kunlun fault are highly consistent with the studies of other major strike-slip faults, such as the San Andreas Fault. The low-velocity and low- Q zone in the KLFZ model is the effect of multiple ruptures along the fault trace of the 2001 Kunlun *M*8.1 earthquake.

ACKNOWLEDGMENTS

This research is sponsored by the National Natural Science Foundation of China (No. 40474019 and No. 40334041), the Special Project of Social Public Welfare Research (No. 2002DIA10001) and the International Cooperation Program (Grant No. 2003DF000011) in the Ministry of Science and Technology of China. Sincere thanks are due to R. W. Graves, who provided his staggered-grid finite-difference code. Reviews by the Editor, Y. Ben-Zion, and two anonymous reviewers led to significant revisions of the submitted manuscript. The authors are grateful to them. The authors also sincerely appreciate the help of field work from China Seismological Bureau, Qinghai Seismological Bureau and Golmud Seismological Bureau.

REFERENCES

- Aki, K., 1979. Characterization of barriers on an earthquake fault, *J. geophys. Res.*, **84**, 6140–6148.
- Aki, K. & Richards, P.C., 2002. *Quantitative Seismology*, 2nd edn, University Science Books, Sausalito, CA.

- Assumpcao, M., Bamford, D. & LISP, V., 1978. Studies of crustal shear waves, *Geophys. J. R. astr. Soc.*, **54**, 61–73.
- Ben-Zion, Y., 1998. Properties of seismic fault zone waves and their utility for imaging low-velocity structure, *J. geophys. Res.*, **103**, 12 567–12 585.
- Ben-Zion, Y. & Aki, K., 1990. Seismic radiation from an SH line source in a laterally heterogeneous planar fault zone, *Bull. seism. Soc. Am.*, **80**, 971–994.
- Ben-Zion, Y. & Malin, P., 1991. San Andreas fault zone head waves near Parkfield, California, *Science*, **251**, 1592–1594.
- Ben-Zion, Y. & Sammis, C.G., 2003. Characterization of fault zones. *Pure appl. Geophys.*, **160**, 677–715.
- Ben-Zion, Y. *et al.*, 2003. A shallow fault zone structure illuminated by trapped waves in the Karadere-Duzce branch of the North Anatolian Fault, Western Turkey, *Geophys. J. Int.*, **152**, 699–717.
- Braile, L.W., Smith, R.B., Keller, G.R., Welch, R.M. & Meyer, R.P., 1974. Crustal structure across the Wasatch Front from detailed seismic refraction studies, *J. geophys. Res.*, **79**, 2669–2677.
- Cerveny, V. & Psencik, I., 1984. SEIS83-numerical modeling of seismic wavefield in 2-D laterally varying layered structures by the ray method, in: *Documentation of Earthquake Algorithm*, pp. 36–40, ed. Engdahl, E.R., Rep. SE-35, World Data Center (A) for Solid Earth Geophysics, Boulder, Colo.
- China Seismological Bureau, 2003. *Album of the Kunlun Pass W. Ms 8.1 Earthquake*, China Seismological Press, Beijing.
- Cormier, V.F. & Spudich, P., 1984. Amplification of ground motion and waveform complexity in fault zones: Examples from the San Andreas and Calaveras faults, *Geophys. J. R. astr. Soc.*, **79**, 135–152.
- Christensen, N.I. & Mooney, W.D., 1995. Seismic velocity structure and composition of the continental crust: A global view, *J. geophys. Res.*, **100**, 9761–9788.
- Cui, Z., Li, Q., Wu, C., Yin, Z. & Liu, H., 1995. Crustal structure of the Golmud-E'jinaqi geosciences transect and its tectonic implication, *Geophys. Res. China*, **38**(Suppl. 2), 15–28 (in Chinese).
- Dziewonski, A., Bloch, S. & Landisman, M., 1969. A technique for the analysis of transient signals, *Bull. seism. Soc. Am.*, **59**, 427–444.
- El-Isa, Z., Mechie, J. & Prodehl, C., 1987. Shear velocity structure of Jordan from explosion seismic data, *Geophys. J. R. astr. Soc.*, **90**, 265–281.
- Fertig, J., 1984. Shear waves by an explosive point-source: The earth surface as a generator of converted P-S waves, *Geophys. Prospect.*, **32**, 1–17.
- Fohrmann, M., Igel, H., Jahnke, G. & Ben-Zion Y., 2004. Guided waves from sources outside faults: An indicator for shallow fault zone structure? *Pure appl. Geophys.*, **161**, 2125–2137.
- Giese, P., Prodehl, C. & Stain, A., 1976. *Explosion Seismology: Data and Results*, Springer, Berlin, 429 pp.
- Graves, R.W., 1996. Simulating seismic wave propagation in 3D elastic media using staggered-grid finite differences, *Bull. seism. Soc. Am.*, **86**, 1091–1106.
- Haberland, C. *et al.*, 2003. Modelling of seismic guided waves at the Dead Sea Transform, *J. geophys. Res.*, **108**(B7), 2342, doi:10.1029/2002JB002309.
- Hickman, S.H., Zoback, M.D. & Ellsworth, W.L., 2005. Structure and composition of the San Andreas Fault zone at Parkfield: Initial results from SAFOD Phase 1 and 2, *EOS, Trans. Am. geophys. Un.*, **83**(47), 237.
- Holbrook, W.S., Gajewski, D., Krammer A. & Prodehl, C., 1988. An interpretation of wide-angle compressional and shear wave data in southwest Germany: Poisson's ratio and petrological implications, *J. geophys. Res.*, **93**, 12081–12106.
- Holbrook, W.S., Mooney, W.D. & Christensen, N.J., 1992. The seismic velocity structure of the deep continental crust, in *Continental Lower Crust*, pp. 1–34, eds Fountain, D.M., Arculus, R., Kay, R.W., Elsevier Science Publishers, Amsterdam.
- Institute of Geophysics, China Seismological Bureau, 2002. *Seismic Observation Report of China Seismological Network*, Seismological Press, Beijing (in Chinese).
- Igel, H., Ben-Zion, Y. & Leary, P., 1997. Simulation of SH and P-SV wave propagation in fault zones, *Geophys. J. Int.*, **128**, 533–546.
- Kanamori, H., 1994. Mechanics of earthquakes, *Annu. Rev. Earth Planet. Sci.*, **22**, 207–237.
- Kidd, W.S.F. & Molnar, P., 1988. Quaternary and active faulting observed on the 1985 Academia Sinica-Royal Society Geotraverse of Tibet, *Phil. Trans. R. Soc. Lond.*, **327**, 337–363.
- Lees, J.M. & Malin, P.E., 1990. Tomographic images of P wave velocity variation at Parkfield, California, *J. geophys. Res.*, **95**, 21793–21804.
- Lewis, M.A., Peng, G., Ben-Zion, Y. & Vernon, F.L., 2005. Shallow seismic trapping structure in the San Jacinto fault zone near Anza, California, *Geophys. J. Int.*, **162**(3), 867–881, doi:10.1111/j.1365-246X.2005.02684.
- Li, Y.G. & Leary, P.C., 1990. Fault-zone trapped seismic waves, *Bull. seism. Soc. Am.*, **80**, 1245–1271.
- Li, Y.G., Aki, K., Adams, D., Hasemi, A. & Lee, W.H.K., 1994. Seismic guided waves trapped in the fault zone of the Landers, California, earthquake of 1992, *J. geophys. Res.*, **99**, 11705–11722.
- Li, Y.G., Aki, K., Vidale, J.E. & Alvarez, M.G., 1998. A delineation of the Nojima fault ruptured in the M7.2 Kobe, Japan, earthquake of 1995 using fault-zone trapped waves, *J. geophys. Res.*, **103**, 7247–7263.
- Li, Y.G., Aki, K., Vidale, J.E. & Xu, F., 1999. Shallow structure of the Landers fault zone from explosion-generated trapped waves, *J. geophys. Res.*, **104**, 20257–20275.
- Li, Y.G., Vidale, J.E., Day, S.M., Oglesby, D.D. & the SCEC Field Working Team, 2002a. Study of the 1999 M7.1 Hector Mine, California earthquake fault plane by trapped waves, *Bull. seism. Soc. Am.*, **92**, 1318–1332.
- Lin, A., Fu, B., Guo, J., Zeng, Q., Dang, G., He, W. & Zhao, Y., 2002b. Co-seismic strike-slip and rupture length produced by the 2001 Ms 8.1 Central Kunlun earthquake, *Science*, **296**, 2015–2017.
- Li, Y.G., Vidale, J.E. & Cochran, S.E., 2004. Low-velocity damaged structure of the San Andreas fault at Parkfield from fault-zone trapped waves, *Geophys. Res. Lett.*, **31**, L12S06.
- Li, Y.G., Chen, P., Cochran, S.E., Vidale, J.E. & Burdette, T., 2006. Seismic evidence for rock damage and healing on the San Andreas fault associated with the 2004 M6 Parkfield earthquake. Special issue for Parkfield M6 earthquake, *Bull. seism. Soc. Am.*, **96**, doi:10.1785/0120050803.
- Louie, J.N., Clyton, R.W. & LeBras, R.J., 1988. Three-dimensional imaging of steeply dipping structure near the San Andreas fault, Parkfield, California, *Geophysics*, **53**, 176–185.
- Lyakhovskiy, V. & Ben-Zion, Y., 2008. Scaling relations of earthquakes and aseismic deformation in a damage rheology model, *Geophys. J. Int.*, **172**, 651–662.
- Meissner, R., 1986. *The Continental Crust, a Geophysical Approach*, pp. 426, Academic Press, London.
- Michelini, A. & McEvelly, T.V., 1991. Seismological studies at Parkfield, 1, Simultaneous inversion for velocity structure and hypocenters using cubic B-spline parameterization, *Bull. seism. Soc. Am.*, **81**, 524–552.
- Mooney, W.D., 1989. Seismic methods for determining earthquake source parameters and lithospheric structure, *Geophysical Framework of the Continental United States*, pp. 11–34, eds Pakiser, L.C., Mooney, W.D., Geological Society of America Memoir 172.
- Mooney, W.D. & Ginzburg, A., 1986. Seismic measurements of the internal property of fault zone, *Pure appl. Geophys.*, **124**, 141–157.
- Peltzer, G., Grampe, E. & King, G., 1999. Evidence of nonlinear elasticity of the crust from the Mw 7.6 Manyi (Tibet) earthquake, *Science*, **286**, 272–276.
- Peng, Z. & Ben-Zion, Y., 2004. Systematic analysis of crustal anisotropy along the Karadere-Duzce branch of the north Anatolian fault, *Geophys. J. Int.*, **159**, 253–274.
- Peng, Z., Ben-Zion, Y., Michael, A.J. & Zhu, L., 2003. Quantitative analysis of fault zone waves in the rupture zone of the Landers, 1992, California earthquake: Evidence for a shallow trapping structure, *Geophys. J. Int.*, **155**, 1021–1041.
- Qinghai Seismological Bureau and Institute of Geodynamics, CSB, 1999. *Eastern Kunlun Active Fault Zone*, pp. 186, Seismological Press, Beijing (in Chinese).
- Rovelli, A., Caserta, A., Marra, F. & Ruggiero, V., 2002. Can seismic waves be trapped inside an inactive fault zone? The case study of Nocera Umbra, central Italy, *Bull. seism. Soc. Am.*, **92**, 2217–2232.
- Sambridge, M. & Drijkoningen, G., 1992. Genetic algorithm in seismic waveform inversion, *Geophys. J. Int.*, **109**, 323–342.

- Scholz, C.H., 2002. *The Mechanics of Earthquakes and Faulting*, 2nd edn, Cambridge Univ. Press, New York.
- Sibson, R.H., 2002. Geology of the crustal earthquake source, *International Handbook of Earthquake and Engineering Seismology, Part A*, pp. 455–473, eds Lee, W.H.K., Kanamori, H., Jennings, P.C., Kisslinger, C., Academic Press, San Diego.
- Teng, T.L., 1968. Attenuation of body waves and the Q structure of the mantle, *J. geophys. Res.*, **73**, 2195–2208.
- Thurber, C.H., 1983. Earthquake locations and three-dimensional crustal structure in the Coyote Lake area, central California, *J. geophys. Res.*, **88**, 8226–8236.
- Thurber, C.H., Roecker, S., Ellsworth, W., Chen, Y., Lutter, W. & Sessions, R., 1997. Two-dimensional seismic image of the San Andreas fault in the northern Gabilan Range, central California, Evidence for fluids in the fault zone, *Geophys. Res. Lett.*, **24**, 1591–1594.
- Van Der Woerd, J. et al., 1998. Holocene left-slip rate determined by cosmogenic surface dating on the Xidatan segment of the Kunlun fault (Qinghai, China), *Geology*, **26**, 695–698.
- Van Der Woerd, J. et al., 2000. Uniform slip-rate along the Kunlun Fault: implication for seismic behavior and large-scale tectonics, *Geophys. Res. Lett.*, **27**, 2353–2356.
- Van Der Woerd, J., Meriaux, A.S., Klinger, Y., Ryerson, F.J., Gaudemer, Y. & Tapponnier, P., 2002. The 14 November 2001, $M_w = 7.8$ Kokoxili earthquake in northern Tibet (Qinghai Province, China), *Seism. Res. Lett.*, **73**, 125–135.
- Wang, C.Y., Zeng, R.S., Mooney, W.D. & Hacker, B.R., 2000. A crustal model of the ultrahigh-pressure Dabie Shan orogenic belt, China, derived from deep seismic refraction profiling, *J. geophys. Res.*, **115**(B5), 10857–10869.
- Wang, C.Y., Han, W.B., Wu, J.P., Lou, H. & Chan, W., 2007. Crustal structure beneath the eastern margin of the Tibetan Plateau and its tectonic implications, *J. geophys. Res.*, **112**, B07307, doi:10.1029/2005JB003873.
- Wu, G.J., Gao, R. & Yu, Q.F., 1991. Comprehensive geophysical investigation of the Yadong-Golmud geosciences transect in the Tibetan Plateau, *Acta Geophysica Sinica*, **34**, 552–562 (in Chinese).
- Xu, L.S. & Chen, Y.T., 1999. Tempo-spatial rupture process of the 1997 Manyi, Tibet, China earthquake of $M_s = 7.9$, *Acta Seismologica Sinica*, **12**, 495–506.
- Xu, L.S. & Chen, Y.T., 2005. Temporal and spatial rupture process of the great Kunlun Mountain Pass earthquake of November 14, 2001 from the GDSN long period waveform data, *Sciences in China (D)*, **48**(1), 112–122.
- Xu, X.W., Chen, W.B., Ma, W.T., Yu, G.H. & Chen, G.H., 2002. Surface rupture of the Kunlunshan earthquake ($M_s 8.1$), Northern Tibetan Plateau, China, *Seismol. Res. Lett.*, **73**(6), 884–892.
- Yin, A. & Harrison, T.M., 2000. Geologic evolution of the Himalayan-Tibetan orogen, *Annu. Rev. Earth Planet. Sci.*, **28**, 211–280, doi:10.1146/annurev.earth.28.1.211.
- Zhao, K., Zhuang, C.T. & Shen, S.J., 1997. A feedback broadband seismometer applying to digital seismograph network, *Earthquake*, **17**(Suppl), 36–44 (in Chinese).
- Zhu, L., Owens, T.J. & Randall, G., 1995. Lateral variation in the crustal structure of the northern Tibetan plateau inferred from teleseismic receiver functions, *Bull. seism. Soc. Am.*, **85**, 1531–1540.

Copyright of *Geophysical Journal International* is the property of Blackwell Publishing Limited and its content may not be copied or emailed to multiple sites or posted to a listserv without the copyright holder's express written permission. However, users may print, download, or email articles for individual use.